A Self-Absorption Census of Cold H I Clouds in the Canadian Galactic Plane Survey

Steven J. Gibson[1], A. Russell Taylor[1], Lloyd A. Higgs[2], Christopher M. Brunt[3], and Peter E. Dewdney[2]

ABSTRACT

We present a 21cm line H I self-absorption (HISA) survey of cold atomic gas within Galactic longitudes $\ell = 75°$ to $146°$ and latitudes $b = -3°$ to $+5°$. We identify HISA as spatially and spectrally confined dark H I features and extract it from the surrounding H I emission in the arcminute-resolution Canadian Galactic Plane Survey (CGPS). We compile a catalog of the most significant features in our survey and compare our detections against those in the literature. Within the parameters of our search, we find nearly all previously detected features and identify many new ones. The CGPS shows HISA in much greater detail than any prior survey and allows both new and previously-discovered features to be placed into the larger context of Galactic structure. In space and radial velocity, faint HISA is detected virtually everywhere that the H I emission background is sufficiently bright. This ambient HISA population may arise from small turbulent fluctuations of temperature and velocity in the neutral interstellar medium. By contrast, stronger HISA is organized into discrete complexes, many of which follow a longitude-velocity distribution that suggests they have been made visible by the velocity reversal of the Perseus arm's spiral density wave. The cold H I revealed in this way may have recently passed through the spiral shock and be on its way to forming molecules and, eventually, new stars. This paper is the second in a series examining HISA at high angular resolution. A companion paper (Paper III) describes our HISA search and extraction algorithms in detail.

Subject headings: methods: analytical — surveys — ISM: clouds — ISM: general — ISM: kinematics and dynamics — ISM: structure

---

[1]Dept. of Physics & Astronomy, University of Calgary, 2500 University Drive N.W., Calgary, Alberta T2N 1N4, Canada; gibson@ras.ucalgary.ca; russ@ras.ucalgary.ca

[2]Dominion Radio Astrophysical Observatory, Box 248, Penticton, British Columbia V2A 6K3, Canada; Lloyd.Higgs@nrc.ca; Peter.Dewdney@nrc.ca

[3]Department of Astronomy, LGRT 632, University of Massachusetts, 710 North Pleasant Street, Amherst, MA 01003; brunt@roobarb.astro.umass.edu

1. Introduction

1.1. Mapping Cold Galactic H I

The cold ($T \lesssim 100$ K) phase of neutral atomic hydrogen gas (H I) is an important probe of the mass, structure, and evolutionary state of the Galactic interstellar medium (ISM). Although it occupies only a small fraction of the ISM volume (Kulkarni & Heiles 1988), cold H I contains $\sim 30\%$ of the total gas mass near the Sun (Wolfire et al. 2003). On sub-parsec scales, cold H I clouds display significant structure (Gibson et al. 2000, hereafter Paper I; Brogan et al. 2005) that may be shaped by shocks, turbulence, or magnetic fields. On kiloparsec scales, the cold H I distribution may trace spiral structure in the Galactic disk (Gibson 2002; Gibson et al. 2004). Cold H I may even offer a window into the process of molecular condensation. It is often found with molecular gas in the quiescent environments needed for star formation (Knapp 1974), and it can be used to study turbulent diffusion (Willacy, Langer, & Allen 2002) and cosmic-ray dissociation (Li & Goldsmith 2003) inside molecular clouds. But cold H I without apparent molecular gas is also found (Garwood & Dickey 1989; Paper I), sometimes at temperatures too cold for standard equilibrium ISM models to explain easily (Wolfire et al. 2003); such gas may be cooling and forming H_2.

Investigating these issues thoroughly requires mapping cold H I over large areas, but this is not straightforward. The principal H I tracer, 21cm line emission, does not show cold gas conspicuously, since the line brightness is independent of temperature when optically thin and proportional to temperature when optically thick (Gibson 2002). In fact, since H I column densities computed from 21cm line emission presume optically thin conditions, they miss much of the coldest, densest H I and underestimate the total mass. However, the inverse dependence of optical depth on temperature allows cold H I to be readily examined in *absorption*. H I continuum absorption (HICA) studies find that typically 30% of the total H I mass is missed by emission columns in the Galactic plane (Dickey et al. 2003; Strasser & Taylor 2004), with almost 50% missed in some cases (Dickey & Benson 1982). HICA is thus a valuable probe of the cold H I phase, but the discrete nature of most continuum backgrounds compromises HICA's ability to map the cold gas distribution.

A more suitable alternative is H I *self-absorption*[1] (HISA), which arises from H I gas with an excitation temperature colder than the background H I brightness temperature. Since the total Galactic H I brightness is $\lesssim 100 - 150$ K, HISA has a built-in temperature filter

[1]In the convention of 21cm line work, this long-used term (e.g., Wild 1952; Radhakrishnan 1960) does not imply that the absorbing and emitting gas are intermixed or even close together along the line of sight (Burton, Liszt, & Baker 1978), although these possibilities are not excluded.

that allows it to trace cold gas exclusively. Like HICA, HISA requires suitable backgrounds, but bright H I emission is found over large, continuous areas at low latitude. As a result, HISA is an excellent tool for mapping the structure and distribution of cold Galactic H I.

1.2. HISA Observations

A thorough HISA survey of the cold H I population requires high angular resolution, high radial velocity resolution, and broad sky coverage. The first two provide a detailed view of HISA structure, with reduced dilution of spatially and spectrally sharp absorption features, and refined estimation of the unabsorbed H I brightness, as measured near HISA feature edges in space and velocity. The third permits the study of a large population of objects, unbiased by any target preselection (e.g., molecular clouds), allowing the cold H I properties to be examined in the context of the larger environment.

Due to the effort and resources required, a HISA survey incorporating all three ingredients has never been published; the closest approximation is the Boston University Arecibo H I survey, only part of which is Nyquist sampled (Kuchar & Bania 1994; T. M. Bania 2005, in preparation). Two prior Arecibo mapping surveys consisted of longitude-velocity or latitude-velocity strip-maps only (Baker & Burton 1979; Bania & Lockman 1984). Other HISA surveys have targeted known molecular clouds with single-dish telescopes and little or no imaging (Knapp 1974; McCutcheon, Shuter, & Booth 1978; Levinson & Brown 1980; Snell 1981; Sandqvist, Tomboulides, & Lindblad 1988; Li & Goldsmith 2003), and until recently only a few isolated objects have been observed with synthesis telescopes (Radhakrishnan et al. 1972; Chu 1975; Landecker, Roger, & Higgs 1980; Read 1980, 1981; Dewdney & Roger 1982; van der Werf, Goss, & Vanden Bout 1988; van der Werf et al. 1989; Feldt 1993; Schwarz et al. 1995; Lebrón & Rodríguez 1997).

Fortunately, new technological advances have made H I synthesis surveys over large areas possible. One such effort, the Canadian Galactic Plane Survey (CGPS; Taylor et al. 2003), is the basis of this paper. The CGPS combines a hexagonal grid of full-synthesis fields with single-dish observations to enable the detection of all scales of H I structure down to the synthesized beam. The CGPS H I data have a $58'' \times 58''\mathrm{cosec}(\delta)$ beam, 0.824 $\mathrm{km\,s^{-1}}$ velocity sampling, and a field-center noise of $T_{rms} \sim 3$ K in empty channels; T_{rms} doubles when the $107'$ primary beam is filled with 100 K emission, and it can be up to 60% greater between field centers. The initial phase of the survey mapped a $73^\circ \times 9^\circ$ region along the Galactic plane with longitudes $74.2^\circ \leq \ell \leq 147.3^\circ$ and latitudes $-3.6^\circ \leq b \leq +5.6^\circ$ ($+33.9^\circ \leq \delta \leq +68.4^\circ$), and extensions in both ℓ and b have followed. This paper deals solely with the Phase I CGPS, which we shall call simply "the CGPS" for brevity. Paper I

gave a preliminary view of HISA in the CGPS, including many small-scale features masked by beam dilution in single-dish surveys. Larger-scale HISA features have also been found in CGPS data by Higgs & Tapping (2000), Knee & Brunt (2001), and Higgs et al. (2005). Two other major synthesis surveys, the Southern Galactic Plane Survey (SGPS; McClure-Griffiths et al. 2001b) and VLA Galactic Plane Survey (VGPS; Taylor et al. 2002), have abundant and intricate HISA populations as well (McClure-Griffiths et al. 2001a; Kavars et al. 2003; Gibson et al. 2004).

1.3. A Large-Scale HISA Survey

Following the first look at CGPS HISA given in Paper I, this paper presents a large HISA survey over the entire $73^\circ \times 9^\circ$ CGPS. Our intent is to chart all of the cold H I in the CGPS that is readily detectable as HISA so that the feature population can be studied over a wide area with minimal selection bias.

A companion paper (Gibson et al. 2005a; hereafter Paper III) describes the automated algorithms used in this paper to locate HISA features in the H I data cubes and extract them for analysis. Our technique seeks out dark features in the H I data with abundant small-scale structure in space and velocity. This approach succeeds in finding most of the HISA that is conspicuous to the eye. Maps of the detected HISA trace a rich array of cold H I features over the breadth of the CGPS, including a froth of low-amplitude HISA and a number of elaborate complexes of stronger absorption. The weak absorption seems well mixed with the general H I emission and may arise from small turbulent fluctuations in velocity and temperature in the ISM. Many of the stronger absorption features appear to probe cold atomic gas in the velocity reversal of the Perseus spiral arm and may trace evolving material in the arm.

Below, we summarize our method of HISA identification and extraction (§2), present the features it finds in the CGPS (§3), and consider the spatial and velocity distributions of the HISA (§4). Detailed analyses of the properties of the HISA features and their degree of correspondence with molecular gas will be presented separately (Gibson et al. 2005b). Early results from some of this work have been discussed in Gibson (2002).

2. HISA Identification and Extraction

In past HISA studies, visual inspection sufficed for identifying self-absorption features, but the large amount of data in a survey like the CGPS makes this impractical. Visually

identified HISA is also unlikely to be selected in a uniform or repeatable manner. To address these concerns, we have developed an automated means of searching for HISA in 21cm spectral line data. We have also developed a method of interpolating the T_{OFF} brightness around the feature in (ℓ, b, v) space to obtain the best-constrained estimate of the unabsorbed brightness T_U that would be observed at the feature position in the absence of HISA. From this, the absorption amplitude of the feature is obtained as $\Delta T \equiv T_{ON} - T_U$, where T_{ON} is the brightness temperature on the feature, and $\Delta T < 0$. Full discussions of the workings and evaluation of our HISA search and extraction software are presented in Paper III, but we summarize key aspects here.

Our search method is conservative: we seek H I features that can only be identified as HISA. Following the criteria of Paper I, such features have narrower line widths than most emission, steeper line wings, more small-scale angular structure, and a minimum background H I brightness. The last condition excludes narrow gaps between sharp-edged emission features, which are more common in the absence of bright backgrounds. Using a variant of the CLEAN algorithm of Steer, Dewdney, & Ito (1984), we iteratively remove large-scale emission features from the H I data and flag significant negative residuals as HISA. The CLEAN is performed separately in the spectral and spatial domains, and only features satisfying both searches are retained. T_U is then estimated by interpolating the T_{OFF} brightness around the feature in 3-D. HISA detections with $T_U < 70$ K are rejected. Detections where the survey noise is unacceptably high are also rejected as untrustworthy. The CLEAN filtering removes HISA on the largest spectral and spatial scales, but some of this larger structure is recovered by subtracting the flagged absorption from the H I data and rerunning the search. A total of 3 search+extraction iterations were applied to the CGPS data.

The search software was tuned to find as much visually identifiable HISA as possible while minimizing false detections. It was then tested extensively with model H I data containing random backgrounds, absorption features, and noise. The absorption extracted by the software was compared to that put into the models, and the software performance was evaluated as a function of four "observables": ΔT, T_U, $\Delta\theta$, and Δv, where the latter two measure the local angular and velocity widths of features. Within this 4-D parameter space, we measured f_{det}, the fraction of input HISA detected, f_{true}, the fraction of output HISA that represents true detections, and $\Delta\Delta T$, $\Delta\Delta\theta$, and $\Delta\Delta v$, the measurement drifts between input and output ($\Delta T_U = -\Delta\Delta T$).

We found that HISA meeting our design criteria is generally well detected: f_{det} is high for HISA significantly stronger than the noise level, larger than a few beams, narrower than a few $\mathrm{km\,s^{-1}}$, and with $T_U \gtrsim 80$ K. At the same time, the bulk of HISA detections are reliable, with f_{true} near unity in most parts of the parameter space except those occupied

by beam-scale noise fluctuations. Measurement drifts are small in well-detected features, with $|\Delta T|$ and $T_{_U}$ being underestimated by a few K due to contamination of $T_{_{OFF}}$ by faint, undetected HISA near the feature. Where detections are truncated by noise fluctuations or faint $T_{_U}$, the bias may be somewhat larger. $\Delta\Delta\theta$ and $\Delta\Delta v$ are both negative in most cases, since incomplete detection makes features appear smaller and narrower. In practice, these effects manifest as the stronger-absorption cores of HISA features being detected when some weaker-absorption envelopes may be missed.

3. Absorption Amplitude Maps

3.1. Constraints on the Survey Area

The CGPS H I data are released in $5.12^\circ \times 5.12^\circ \times 211\,\mathrm{km\,s^{-1}}$ ($1024 \times 1024 \times 256$) cubes. All 36 of the Phase I cubes were processed with the HISA identification and extraction software described in §2. The results were then merged into a single data set covering the full CGPS[2]. Figure 1 shows side-by-side (ℓ, b) and (ℓ, v) projections of these data, in which ΔT is integrated over v and b respectively. The $\Delta T(\ell, b, v)$ data are sparse enough that most features are readily located in 3-D by comparing the two projections. Figure 1 is divided into four longitude subranges matching those of Figure 7 of Taylor et al. (2003).

3.1.1. Noise Limits

The total area mapped by the 193 overlapping fields of the CGPS is 656.2 deg^2, but this includes synthesis field peripheries with substantial noise. To maximize the reliability of our survey, HISA voxels were required to have CGPS field mosaic weights $w_m \geq 0.382$, the lowest weight that occurs between synthesis field centers. Since $w_m \propto \sigma_{noise}^{-2}$, this allows a maximum noise of 1.618 times the field center value (see Taylor et al. 2003), which is typically $5 - 7$ K for the $T_{_U} \sim 70 - 130$ K levels of our HISA features. Such peripheral clipping and the additional exclusion of $20'$ strips at mosaic edges by the spatial search algorithm (see Paper III, Fig. 3) reduce the search area to 528.3 deg^2 in a region bounded by $75.0^\circ \leq \ell \leq 146.5^\circ$ and $-3.0^\circ \leq b \leq +5.0^\circ$, with complete coverage for $76.0^\circ \leq \ell \leq 145.5^\circ$ and $-2.5^\circ \leq b \leq +4.5^\circ$, except near the bright radio source Cas A ($\ell = 111.7^\circ, b = -2.1^\circ$). Figure 2 marks the boundaries of this area.

[2]Electronic copies of these data are available upon request.

3.1.2. HICA Contamination

Figure 2 also plots contours of 21cm continuum emission (shown in grayscale in Figure 7 of Taylor et al. 2003). Where the continuum is bright, HICA may "contaminate" the cold H I sampled by HISA in two different ways: by adding absorption where the H I background is too faint for HISA, or by allowing warmer gas to contribute to the absorption than HISA would by itself, since the maximum temperature of the absorbing gas is the brightness temperature of the background H I + continuum. Both problems are exacerbated by the spotty nature of most bright continuum emission, which adds artificial absorption structure to the HISA map.

Our HISA identification software excludes sight lines with HICA strong enough for T_{ON} to be significantly less than zero (Paper III). Apart from special cases involving polarization (Kothes, Landecker, & Wolleben 2004), weaker HICA cannot be separated cleanly from the HISA without knowing the properties of the absorbing gas. In the 4-component radiative transfer model of Paper I, the total HISA+HICA amplitude is

$$\Delta T_{tot} \;=\; (T_S - T_C - p\,T_U)\left(1 - e^{-\tau}\right) \quad , \tag{1}$$

where T_S is the "spin" (excitation) temperature of the absorbing gas, τ is its optical depth, p is the fraction of T_U originating behind the absorbing gas, and T_C is the continuum brightness temperature; all of T_C is assumed to originate in the far background for simplicity. The absorption from HISA alone is found by setting $T_C = 0$ in Equation (1), so its fraction of the total is

$$\frac{\Delta T_{HISA}}{\Delta T_{tot}} \;=\; \frac{T_S - p\,T_U}{T_S - T_C - p\,T_U} \quad . \tag{2}$$

For $T_{OFF} = 100$ K, $T_C = 20$ K, and $p \leq 1$, this ratio is ≤ 0.71 for $T_S = 50$ K and ≤ 0.82 for $T_S = 10$ K. Higher fractions obtain if some of the continuum emission lies in front of the absorbing gas. Constraining the radiative transfer adequately to separate HISA from HICA is beyond the scope of this paper. Fortunately, most detected CGPS HISA is largely HICA-free, with only a smooth, faint $T_C \sim 5$ K background from Galactic synchrotron and cosmic microwave background radiation. The two most significant exceptions are a small area around the bright H II region W3 ($\ell = 133.81°, b = +1.22°$; e.g., Normandeau 1999) and a larger area in the extensive Cygnus X complex of H II regions and supernova remnants ($77° \lesssim \ell \lesssim 83°, -1° \lesssim b \lesssim +3°$; e.g., Wendker, Higgs, & Landecker 1991). The bulk of the remaining HICA is in compact features scattered across the CGPS area (Fig. 2; see Strasser & Taylor 2004 for a survey). A prominent example is the ultracompact H II region

DR 7 ($\ell = 79.32°, b = +1.29°$; Wendker & Wrigge 1996), which produces HICA over a wider velocity range than the HISA near $v_{LSR} \sim 0$ km s^{-1} in Figure 1.

3.1.3. T_U Restriction

In addition to the boundary marked in Figure 2, HISA detections are also restricted by the requirement that $T_U \geq 70$ K, since HISA needs bright H I backgrounds for it to arise and to be clearly detected (§2). The effects of this constraint are illustrated in Figure 3, which plots approximate $T_U = 70$ K contours over (ℓ, b) and (ℓ, v) maps of detected HISA. These contours are taken from T_{max} maps of 20′-smoothed CGPS H I emission, where T_{max} is the brightest value along the projected axis, thus indicating positions where suitable HISA backgrounds may occur. The actual T_U used in the HISA identification software is difficult to show in 2-D, but these smoothed maps give a reasonable indication of where HISA detections are possible. Their 70 K levels correspond closely to a number of sharp edges of the HISA distribution. The cold H I gas traced by the HISA may continue beyond these apparent edges in many cases. Given the large number of Galactic H I sight lines and velocities for which $T_U < 70$ K, it is important to emphasize that the detected HISA population may represent only a small subset of the total cold H I population. The (ℓ, b) area enclosed by this T_U contour is 398.0 deg^2. In §4, we will consider the fraction of this area covered by detected HISA of different strengths, along with other survey completeness issues.

3.2. General Appearance

A detailed analysis of the general HISA distribution is given in §4, and a full discussion of HISA gas properties and correspondences with molecular material will be presented in a separate paper. However, a few points require initial comment.

Figure 1 shows a broad swath of HISA over the entire length of the survey. The detection of this HISA immediately confirms that gas radial velocities do not change monotonically with distance in the outer Galaxy (e.g., from pure differential Galactic rotation), since any HISA requires background H I emission at the same radial velocity as the absorbing gas. The detection of so *much* HISA over such a large area indicates this situation is widespread.

Low-amplitude HISA appears almost ubiquitous, arising nearly everywhere that T_U is bright enough for HISA detection (Fig. 3). By contrast, darker HISA is more concentrated in both space and velocity, collecting in complexes that often resemble molecular clouds in their structure. Quite strong absorption is found at velocities consistent with both Local

and Perseus arm gas, although at very different longitudes. In this paper, "strong" simply means large $|\Delta T|$, which could be caused by a variety of factors in Equation (1).

The strongest HISA is at low velocities and low longitudes, where it coincides with three large CO complexes described by Dame & Thaddeus (1985): the nearby Cyg OB7 and Cyg Rift complexes and the more distant Cyg X complex that lies beyond the Rift along the tangent of solar motion. The Local arm ($v_{LSR} > -20\,\mathrm{km\,s^{-1}}$) also has HISA at higher longitudes, including the Local HISA Filament of Paper I, but this is generally much weaker. Whether there is less cold H I here is unclear, since $T_U < 70$ K in many areas.

Strong HISA is also found in the Perseus arm ($-20\,\mathrm{km\,s^{-1}} > v_{LSR} > -70\,\mathrm{km\,s^{-1}}$), mostly at high longitudes. The Perseus HISA Complex of Paper I is now revealed as one of a chain of HISA complexes over a large longitude range. Many sight lines within these detected HISA structures have no corresponding CO detection (Paper I), but the HISA velocity distribution is close to that of Roberts' (1972) Perseus arm spiral shock (Gibson 2002), a point we shall revisit in §4.

We find little HISA of any kind for $v_{LSR} < -70\,\mathrm{km\,s^{-1}}$, and only then for $\ell \lesssim 100°$. This HISA is probably in the Outer arm, although the Outer/Perseus boundary is difficult to determine for $90° \lesssim \ell \lesssim 100°$. In this part of the Galaxy, HISA detections are limited by $T_U < 70$ K in most areas (Fig. 3), and where $T_U > 70$ K, much of the background H I emission is too finely structured for our search to detect large-scale HISA. As a result, the large HISA shell of Knee & Brunt (2001) is missed, and only a handful of small features are found. More Outer-arm HISA may remain undetected, and still more cold H I may lack sufficient background emission to self-absorb at all.

3.3. Catalog of Major Features

The high resolution and large area of the CGPS allow the thorough mapping of known HISA features and the discovery of many new ones. We define "features" as HISA voxel (volume-pixel) clusters in (ℓ, b, v) that may or may not correspond to physical "clouds". Cautious interpretation is required, because shadow images do not give a complete picture of reality (Plato 360 BC). Our HISA features may arise from discrete clouds of cold H I, from cold H I concentrations within H_2 clouds, from portions of either where the background H I is bright enough for HISA to arise, or from sight-line superpositions of any of these sharing the same radial velocity.

We have compiled a catalog of the most significant HISA features found by our search algorithms in the CGPS. Using the full-survey $\Delta T(\ell, b, v)$ data cube (§3.1), we identified

contiguous groups of HISA voxels as features, in the same fashion used for T_U estimation. To minimize HICA contamination, all sight lines with $T_C > 20$ K were excluded. This process identifies thousands of features, most of which are small, low-amplitude "fluff". The larger, darker features have complex structure that often intertwines with or surrounds neighboring features in 3-D. Since such cases suggest a physical relationship, we have simplified the catalog by merging any two features together if the (ℓ, b, v) boxes containing each feature overlap and both features satisfy a minimum size requirement. Each feature to be merged must have a HISA (ℓ, b, v) volume of $\geq 0.1\,\mathrm{deg^2\,km\,s^{-1}} = 4851$ CGPS voxels. This restriction keeps the widespread fluff from joining all of the detected HISA into a few unrealistically large features that, e.g., include HISA in both the Local and Perseus arms.

The most significant features in this merged catalog, defined as those for which the HISA volume is also $\geq 0.1\,\mathrm{deg^2\,km\,s^{-1}}$, are marked in Figure 4. There are 69 such features. If we apply the §3.2 criteria for spiral arm membership, 11 features are Local arm, 50 are Perseus arm, and 8 are Outer arm members. All 69 contain at least some high-$|\Delta T|$ voxels, but we do not require feature voxels to have a minimum $|\Delta T|$, since this would identify only feature "cores" rather than whole features. ΔT varies across even the most obvious and coherent features, and strong HISA voxels are almost always enveloped in weaker HISA, especially near feature (ℓ, b, v) edges.

Table 1 lists these Galactic HISA (GHISA) features with measurements of position, extent, (ℓ, b, v) volume, (ℓ, b) area, 3-D integrated absorption, mean and maximum absorption, mean T_U, and three "diagnostics" of completeness and reliability described in §3.4. Derived properties like T_S and N_{HISA} will be considered in a separate paper. The features do not fill their extents solidly; volume filling factors, defined as the volume of HISA voxels divided by the product of the ℓ, b, and v extents, are $\sim 3 - 30\%$, with the larger features having lower filling factors on average. This clumpiness is also reflected in the *contiguous* extents, which although not tabulated are $\sim 2' - 5'$ and $\sim 2 - 3\,\mathrm{km\,s^{-1}}$ on average, and $\lesssim 12' - 30'$ and $\lesssim 5 - 8\,\mathrm{km\,s^{-1}}$ in all but the largest 3 or 4 features. The total HISA volume detected in the CGPS is $214.98\,\mathrm{deg^2\,km\,s^{-1}}$, of which 54.5% is in the features of Table 1. The total CGPS HISA integrated absorption is $-2791.4\,\mathrm{K\,deg^2\,km\,s^{-1}}$, of which the listed features account for 66.2%.

A comparison against past HISA studies in the CGPS region shows that ours reproduces most prior detections while yielding an abundance of new features. Table 1 notes past observations of each feature, and Table 2 summarizes previous HISA work in the CGPS region, including the numbers of past features we have found. Of those that we miss, only two from Read (1980) have $T_U > 70$ K; these have $T_U \sim 85$ K instead, where model tests in Paper III show that our detection sensitivity is high but not 100%. More striking is

that the majority of CGPS features in Table 1 have *no* prior detections in the literature. Although the five most conspicuous features were previously known, most features with volumes of $\lesssim 1\,\mathrm{deg}^2\,\mathrm{km\,s}^{-1}$ and absolute integrated absorptions of $\lesssim 10\,\mathrm{K\,deg}^2\,\mathrm{km\,s}^{-1}$ are new detections. Altogether, only 11 of the features in Table 1 were detected before the CGPS, and only 7 were even partially mapped. None has been mapped as thoroughly as in the CGPS.

A few caveats on the interpretation of these features should be emphasized. First, as noted above, velocity crowding may superpose unrelated absorption along the line of sight, especially near the Local-arm tangent in Cygnus ($75^\circ \lesssim \ell \lesssim 90^\circ, |v_{LSR}| \lesssim 20\,\mathrm{km\,s}^{-1}$). Second, despite the merging of some proximate features, T_U variations may artificially fragment large clouds into multiple features or limit their apparent extent, and the survey edges themselves may truncate some features (e.g., GHISA 079.88+0.62+02, GHISA 091.90+3.27−03, GHISA 145.01+0.46−35, or GHISA 145.81+0.96−36). Finally, the CGPS HISA has a very complex structure, and feature definitions under such circumstances are somewhat subjective. In particular, the choice of merging criteria affects the size and number of major features identified, since if smaller features are allowed to merge, fewer and larger features result. We sought criteria that mimic the eye's identification of features. These criteria were applied algorithmically to ensure precise measurements and uniform treatment.

3.4. Reliability and Completeness

The software performance measures f_{det} and f_{true} can be used to assess the reliability and completeness of particular HISA feature detections. For reliability, the observables ΔT, T_U, $\Delta\theta$, and Δv are measured at each HISA voxel (ℓ, b, v) position, and the f_{true} value corresponding to these coordinates in the 4-D parameter space is assigned to $f_{true}(\ell, b, v)$. For each feature in Table 1, we determined the fractions of its HISA volume and 3-D integrated absorption that are reliably detected as

$$\eta_V \quad = \quad \frac{1}{N_{voxels}} \sum_{n=1}^{N_{voxels}} f_{true}(\ell_n, b_n, v_n) \tag{3}$$

and

$$\eta_{\Delta T} = \frac{\sum_{n=1}^{N_{voxels}} f_{true}(\ell_n, b_n, v_n) \cdot \Delta T(\ell_n, b_n, v_n)}{\sum_{n=1}^{N_{voxels}} \Delta T(\ell_n, b_n, v_n)} , \quad (4)$$

respectively. For the features listed, $0.64 \leq \eta_V \leq 0.98$ and $0.68 \leq \eta_{\Delta T} \leq 0.98$, with respective medians of 0.86 and 0.90. For the survey as a whole, $\eta_V = 0.80$ and $\eta_{\Delta T} = 0.86$. Since f_{true} increases with $|\Delta T|$, $\eta_{\Delta T} \geq \eta_V$ generally, and features with stronger $\langle \Delta T \rangle$ typically have greater reliability fractions.

A similar analysis of detection completeness in terms of f_{det} is not possible, because convergent drifts (e.g., $\Delta\Delta\theta \propto -\Delta\theta$) prevent the recovery of the HISA input properties ($\Delta T_{in}, T_{U\,in}, \Delta\theta_{in}, \Delta v_{in}$) upon which f_{det} depends. However, completeness can be partially assessed in terms of the measured property $T_{U\,out}$; for features of appreciable size and strength, ΔT_U converges symmetrically about $T_U = 80$ K (Paper III), and thus $T_{U\,out} \sim T_{U\,in}$ near 80 K. Table 1 lists $\langle T_U \rangle$, the average $T_{U\,out}$ per voxel, and ϕ_U, the fraction of voxels for which $T_{U\,out} \geq 80$ K. $f_{det} > 0.8$ for reasonably strong features with $T_{U\,in} > 80$ K but declines rapidly for lower $T_{U\,in}$ (Paper III). Although the amount of undetected HISA cannot be quantified, $1 - \phi_U$ gives the fraction of each feature lying where significant HISA might be missed. For example, GHISA 139.01+0.96−40 (the Perseus HISA Complex of Paper I) offers few opportunities to hide strong, undetected HISA. By contrast, GHISA 091.90+3.27−03 has a much lower ϕ_U, and its high-latitude edge is definitely truncated by $T_U < 70$ K. For the entire CGPS HISA set, $\langle T_U \rangle = 92.29$ K and $\phi_U = 0.75$.

3.5. A Remarkably Large, Strong Feature

GHISA 091.90+3.27−03 is one of the most striking HISA features in the CGPS, as shown in Figures 1, 4, and 5. It has the strongest maximum absorption (−80.72 K) in the survey and the strongest average absorption (−24.02 K) of any major feature. It also has the largest area of apparent "solidity", with contiguous HISA extents of $\lesssim 2^\circ$ in ℓ and b. This dark center covers a few square degrees, but it is surrounded by subtle knots and filaments over much larger area, and the feature can even be traced beyond the CGPS boundaries to $b \sim +6^\circ$ in the single-dish surveys of Hartmann & Burton (1997) and Higgs & Tapping (2000). As indicated in Tables 1 & 2, GHISA 091.90+3.27−03 has been studied by several groups and mapped with 25m-class telescopes. It coincides with the dust cloud complex Kh 141 (Khavtassi 1960) and many Lynds (1962) dark nebulae, including LDNe 999, 1002,

1005, and 1029. It may also be associated with other dust clouds over a wider area, since it appears to be part of the large Cyg OB7 giant molecular cloud complex mapped in ^{12}CO by Dame & Thaddeus (1985). Its HISA-CO correspondence is illustrated in Figures 5 and 6. This feature may be related to the even larger, but more diffuse, GHISA 079.88+0.62+02 complex to the west, which also has significant dust content (e.g., LDN 906).

GHISA 091.90+3.27−03 appears dark, cold and quiescent. In many areas it has $T_{ON} \sim 30-40$ K, $\Delta T \sim -50$ K, and a line full width at half maximum (FWHM) of $\Delta v \sim 2.5$ km s^{-1}; a few of the darkest HICA-free knots have $T_{ON} \sim 20-30$ K and $|\Delta T| \sim 60-70$ K. The small white $6' \times 6'$ box in Figure 5 marks an area of fairly typical absorption. For the 4-component radiative transfer geometry of Paper I, the box average values of $T_C = 7.7$ K, $T_{ON} = 45.8$ K, and $T_U = 92.6$ K imply $T_S \leq 53.5$ K for $p \leq 1$ and $\tau \leq \infty$. Since the HISA line does not appear strongly saturated, more reasonable upper limits are probably $T_S \leq 46.2-51.1$ K for $\tau \leq 2-3$. If $p \sim 1$, as seems likely for such a conspicuous feature, lower limits of $T_S \geq 2.73$ K or 10 K imply $\tau \geq 0.65$ or 0.75, respectively. These four (T_S, τ) combinations yield $N_{HI} \sim 0.086$, 0.35, 4.4, and 7.4×10^{20} cm^{-2}. Previous authors have found $N_{HI} = 1.53$ (Knapp 1974), 0.8 (Simonson & van Someren Greve 1976), and 0.1 to 2.0×10^{20} cm^{-2} (Saito et al. 1981) in different parts of the feature. However, the gas mass is probably dominated by H_2. For a mean molecular weight per H_2 molecule of $2.76\, m_H$, Dame & Thaddeus's (1985) results imply an average molecular column of $N_{H_2} \sim 2.3 \times 10^{21}$ cm^{-2}. Our measured HISA column represents only $\sim 0.19-14\%$ of the mass in the total gas column. Dame et al. (1987) estimated the total Cyg OB7 mass as $\sim 7.5 \times 10^5$ M$_\odot$ for a distance of ~ 800 pc.

4. HISA Distribution Analysis

We now consider general trends in the distribution of HISA in the CGPS and their significance. Of particular interest is the relationship between HISA and Galactic structure. We begin with a quantitative discussion of how common HISA is in our survey and what implications this may have for the general picture of the interstellar medium.

4.1. Covering and Filling Fractions

HISA is found in 3.8% of the CGPS voxels that have $T_U > 70$ K, $T_C \leq 20$ K, and adequate mosaic weighting as defined in §3.1.1. 21% of the (ℓ, b) sight lines passing through this searchable volume have detected HISA, and 47% of the (ℓ, v) positions have detected HISA. A relatively small part of the CGPS volume is searchable for HISA, because T_U is high

only in particular regions. However, this portion is still large enough to explore significant characteristics of the HISA distribution in the outer Galaxy. Detection reliability does not significantly affect these results, since $\eta_V = 0.80$ for the full survey (§3.4).

A 3.8% occupation of the (ℓ, b, v) volume may seem low, but in fact this is quite a large fraction: it implies a linear filling factor of $0.038^{1/3} \sim 0.33$ in each dimension for a uniformly random distribution. These values are almost certainly lower limits, since $f_{det} \ll 1$ for $|\Delta T| \ll T_{rms}$, and the abundance of HISA with $|\Delta T| \sim T_{rms}$ (Paper III, Fig. 11) suggests that fainter HISA may be at least as common as HISA at the noise level.

Figure 7 plots the relative incidence of all CGPS HISA voxels with $|\Delta T|$ above a given threshhold. Curves are given for all voxels and for those with $f_{true} \geq 0.90$ and 0.99. The latter two respectively eliminate about one-half and about two-thirds of the total voxel count, mostly at the weak $|\Delta T|$ end where noise contamination is significant. These curves may be rescaled by the occupation fractions listed above to find the fraction of the survey that contains HISA of a particular minimum strength. For example, the volume occupied by reasonably strong HISA with $|\Delta T| > 25$ K is $\sim 10\%$ that of the total HISA population, while HISA with $|\Delta T| > 50$ K accounts for less than 1% of the total.

Simplisticly, we might assume that the HISA census is complete above some $|\Delta T|$ level and extrapolate linearly in log space to lower $|\Delta T|$ to find the amplitude for which the volume filling reaches 100%. E.g., for $|\Delta T|_{complete} \sim 10$ K, we find $|\Delta T|_{filled} \sim 0.1$ K. This extrapolation is not very trustworthy, since it neglects $\Delta\Delta T$ and the more complicated dependences of f_{det}, but it suggests that at low enough (sub-Kelvin) amplitudes, HISA may be truly ubiquitous. Previously, Dickey & Lockman (1990) proposed that faint HISA may cause much of the structure in low-latitude Galactic emission profiles, and Dickey et al. (2003) have argued that HISA occurs in most H I spectra, even if it is not always detectable. Our CGPS HISA census is consistent with these views. At the very least, our survey approaches the confusion limit for HISA detections.

4.2. Weak and Strong HISA

As noted above, HISA with low $|\Delta T|$ is more frequent and more smoothly distributed, while stronger HISA is more rare and more clumped into distinct features. This behavior can be inferred from the ΔT maps in Figure 1, the incidence curves in Figure 7, and the loose $(\Delta T, \Delta\theta)$ and $(\Delta T, \Delta v)$ property correlations in Paper III, Figure 11.

Figure 8 shows the relationship between HISA amplitude and scale more explicitly. Here we plot the RMS dispersions σ_ρ and σ_v of the angular and velocity separations between voxel

pairs in the survey. For every HISA voxel in every CGPS mosaic, the distances to its HISA neighbors along lines of constant ℓ, b, and v were measured, and RMS variations of these measurements were binned by $|\Delta T|_{min}$, the absolute amplitude of the fainter of the two voxels in question. The results, combined for all 36 mosaics, show that weak HISA is more diffusely distributed than strong HISA in both space and velocity. This is not a contradiction of the loose correlation of $|\Delta T|$ with $\Delta\theta$ and Δv in Paper III, Figure 11, since those measured *contiguous* rather than general extent. Instead, the two trends together imply that strong HISA is concentrated into more solid complexes, while weak HISA is spread out in a more porous fashion.

The maximum dispersion scales for the weakest HISA are $\sim 2^\circ$ and $\sim 5\,\mathrm{km\,s^{-1}}$. Once $|\Delta T|_{min}$ exceeds the H I noise level of $\sim$ 6 K, both dispersions drop steadily, with the steepest descent near $\sim$ 20 K. At higher amplitudes, the descent slows and approaches pseudo-asymptotes of $\sim 0.75^\circ$ and $\sim 0.8\,\mathrm{km\,s^{-1}}$ The former is a typical scale for strong HISA features, while the latter corresponds to a 1-channel separation. Above $\sim$ 65 K, angular coherence is lost, the features break into smaller pieces that quickly approach the beam scale, and even 1-channel separations start dropping out when only the maximum absorption channel is sampled. When converted to Gaussian FWHM, the maximum velocity scale approaches the velocity width of the brightest part of a spiral arm in H I emission, and the minimum velocity scale approaches the narrowest linewidths that can be sampled by the CGPS. Angular FWHM are less physically meaningful since the HISA angular structure is complex, but the maximum angular scale is consistent with the $\sim 5^\circ$ size of the CGPS mosaics in which the measurements were made, implying that the weakest HISA has no preferred angular distribution either. Thus, the general trend in both angle and velocity is from weak HISA "fluff" (§3.3) dispersed over the entire measurable area down to discrete, strong HISA features.

The curves in Figure 8 include the entire CGPS HISA data set, but similar trends are seen in different spiral arms when analyzed separately, or at different longitudes in different mosaics. Only the range of strongest absorption and the scale of maximum dispersion change from one location to another. For example, the Local-arm dispersions are larger in both angle and velocity than the Perseus-arm dispersions, and more strong HISA is found in the Local arm, at least in GHISA 079.88+0.62+02 and GHISA 091.90+3.27−03.

4.3. Probing the Gas Kinematics

HISA offers a unique opportunity to study gas motions in the outer Galaxy, because its radiative transfer requires background emission at the same radial velocity as the absorbing

H I. HISA detections with $90° < \ell < 270°$ require departures from pure circular differential rotation, which predicts only one distance per v_{LSR} in this longitude range, apart from the degeneracy at $\ell = 180°$. Two types of CGPS HISA are found: (1) strong HISA with its accompanying weak (ℓ, b, v) envelopes, and (2) unassociated "fluff" that makes up the rest of the weak HISA population. We suggest that these two types are produced by different mechanisms.

4.3.1. Turbulence

Turbulence adds small-scale, random perturbations to the Galactic velocity field. These are likely to be very common but should have small velocity amplitudes and little spatial coherence. Turbulence may also produce cold gas for absorption via departures from equilibrium conditions (e.g., Sánchez-Salcedo, Vázquez-Semadeni, & Gazol 2002; Jenkins 2004). We propose that turbulent (T, v) fluctuations are the source of the weak HISA "fluff" in the CGPS. The fluff lacks coherent large-scale structure, and it occurs in all parts of the CGPS where $T_U > 70$ K, suggesting that it is ubiquitous and well-mixed with the general H I.

Turbulence cannot explain the strong HISA and weak envelopes; this absorption is concentrated into discrete and often large-scale features with well-defined edges. Although brighter T_U makes it easier to see, such HISA does not appear everywhere that T_U is bright enough, so a more organized process than turbulence is needed. The large amplitude of strong HISA is also problematic for the turbulent explanation. High $|\Delta T|$ can result from a high T_C, T_U, τ, or p or a low T_S (Eq. 1). High T_C is rare in CGPS HISA, and we have excluded it where it might affect our analyses. ΔT and T_U are poorly correlated at best (Paper III, Fig. 11), and neither T_U nor p is likely to change abruptly and frequently enough to produce the sharp edges of strong HISA features. Thus strong, discrete HISA must arise from significant changes in τ, T_S, or both. In practice, these absorption enhancements resemble clouds or cloud complexes.

4.3.2. Spiral Density Waves

Spiral density waves add large-scale, organized perturbations to the Galactic velocity field. These are less common than turbulent fluctuations but should have large velocity amplitudes and significant spatial coherence. They may also be a natural source of cold gas. Spiral waves and their associated shocks have long been thought to drive the formation of dense interstellar clouds and massive stars in galactic disks (Lin & Shu 1964; Roberts

1969; Shu et al. 1972), but the full details of the gas dynamics and evolution are complex and difficult to study. In face-on external galaxies, spiral structure is simple to observe, but spatial resolution is limited by distance (e.g., M81: Adler & Westpfahl 1996). By contrast, spatial resolution is much better in the Milky Way, but our internal perspective makes the line of sight geometry difficult to untangle. HISA's sensitivity to velocity reversals is an asset in this situation.

The nearby Perseus arm gives a detailed view of spiral structure and the density wave phenomenon. Roberts (1972) modeled the gas distribution and kinematics in the Perseus spiral shock. Figure 9 illustrates his model's gas density and velocity vs. distance along the line of sight and the (ℓ, v) distribution of the gas passing through the arm. HICA studies have presented evidence in support of this model in a few sight lines toward bright continuum sources (Greisen 1973; Greisen & Lockman 1979; Frail & Hjellming 1991; Normandeau 1999; Kothes & Kerton 2002; Brunt et al. 2002). A more complete picture of the velocity reversal is possible with HISA, which has a much more extensive background than HICA. In the CGPS, strong Perseus HISA is visible over a wide area (e.g., Fig. 1), as would be expected for a neighboring spiral arm.

Figure 10 compares the (ℓ, v) distribution of strong ($|\Delta T| > 20$ K) HISA to the spiral "shock ridge" of Roberts (1972). In his model, the gas slows as it enters the arm shock, reaches a maximum negative-velocity departure from the standard rotation curve speed, and then rebounds toward a positive-going "velocity hill" and the normal rotation speed as it moves on through the rest of the arm and out the back (Fig. 9). We propose that the strong HISA is in or slightly downstream of the shock ridge, the point just behind the shock where the gas is densest, and that H I emission on the far side of the velocity hill serves as a background with the same velocity as the absorbing gas. In support of this assertion, most of the strong Perseus HISA lies on the shock ridge or at more positive velocities for $110° \lesssim \ell \lesssim 145°$ (Fig. 10). Considering that the shock model does not address structural inhomogeneities in the ISM (e.g., Roberts 1993 and references therein), the agreement is quite reasonable; even without prior lumpiness, the shock process itself is expected to introduce some (ℓ, v) structure in the cold gas distribution (Koyama & Inutsuka 2002).

The Local arm is a more ambiguous case. Its two largest features, GHISA 079.88+0.62+02 and GHISA 091.90+3.27−03, are associated with known CO complexes either near the Sun or along the Local arm tangent. The local CO clouds are identified with the Great Rift system of dust clouds (Dame & Thaddeus 1985), which may be related to a ring of expanding material in Gould's Belt (Lindblad 1967; Lindblad et al. 1973). Alternatively, GHISA 091.90+3.27−03 has been suggested to trace a spiral shock in the Local arm (Simonson & van Someren Greve 1976). This scenario conflicts with that of a Local arm shock in the

Galactic center direction (Quirk & Crutcher 1973), but it is consistent with stellar streaming results (Sitnik & Mel'Nik 1999) and naturally explains the presence of background H I emission with the same velocity. However, the Local arm is probably not a major spiral feature, and the dynamics of its stars and gas may instead have been shaped by passage through a "real" spiral arm 100 Myr ago (Olano 2001).

Whichever picture is correct, the presence of background emission at the right velocites must be explained. While the tangent of Solar motion enhances HISA visibility in some areas, it is not clear that the tangent can provide adequate backgrounds for all of the strong Local HISA; e.g., most of GHISA 091.90+3.27−03 has $\ell > 90°$. A Local spiral density wave shock might provide backgrounds at such longitudes, but no quantitative model predictions are available to compare against the CGPS HISA data.

As a general caveat, we note that one well-organized shock per arm may be simplistic: non-grand-design galaxies may have more flocculent shock structure, as suggested by the multiplicity of dust lanes in *Hubble Space Telescope* images of the backlit galaxy NGC 3314 (Keel & White 2001), and even some presumably grand-design spirals may be more complicated (e.g., M51: Henry et al. 2003). The Milky Way is unlikely to be a grand-design spiral, and arguments for multiple shocks in the Perseus arm H I data have been made (Brunt et al. 2002).

HISA features in the inner Galaxy have also been proposed to trace spiral shock material (Sato et al. 1992; Minter et al. 2001; McClure-Griffiths et al. 2001a). More recently, Gibson et al. (2004) reported HISA tracing what appears to be several spiral arms over a large longitude range in the inner Galaxy. These results will be presented in more detail in a separate paper on HISA mapped with the VLA Galactic Plane Survey (S. J. Gibson et al., in preparation).

4.4. An Evolutionary Scenario

Strong HISA requires high τ, low T_s, or both (§4.3.1). The strong Perseus HISA (ℓ, v) distribution appears to trace cold H I immediately downstream of the spiral shock described by Roberts (1972). Passage through a spiral density wave could cause a drop in gas temperature and an increase in density relative to the ambient diffuse atomic medium.

In the classical picture, neutral atomic gas enters the trailing edge of a spiral arm and is decelerated and compressed in the spiral shock; its increased density then leads to rapid cooling, H_2 condensation (e.g., Koyama & Inutsuka 2000; Bergin et al. 2004), and star formation. Elements of this process have been studied by Heyer & Terebey (1998) in CO

and H I emission in the W3/4/5 region of the Perseus arm, and HISA in this area has been proposed to trace sites of molecular formation (Hasegawa et al. 1983; Sato 1990). The CGPS allows this phenomenon to be investigated over a much wider area. Since the Perseus arm HISA is at the right velocity to trace the cold H I that may be forming H_2, and it often lacks CO detections at the same positions (Gibson et al. 2000; Gibson 2002), it may probe the atomic-to-molecular phase transition in the spiral shock environment, or at least H_2 clouds that have not yet formed CO, which could take much longer (Bergin et al. 2004).

Alternatively, density waves may only concentrate pre-existing molecular gas rather than causing an actual phase transition (Vogel, Kulkarni, & Scoville 1988; Pringle, Allen, & Lubow 2001). In this picture, HISA does not arise from "pre-molecular" clouds, but instead from purely atomic cold H I clouds or trace H I in preexisting H_2 clouds that have been "piled up" by the spiral density wave without undergoing a phase change. Tilanus & Allen (1991) argued that this is occurring in M51, where the peak H I brightness in the arms falls slightly "downstream" of the densest regions traced by CO and nonthermal radio continuum emission. However, they noted that their interpretation could be altered if the densest regions contained cold, finely-structured H I, which would not dominate the brightness temperature. Our CGPS HISA results indicate that this is quite plausible. Tilanus & Allen's (1991) H I observations were not sensitive to spin temperatures of $14 - 45$ K, which are similar to those found for strong Perseus HISA in Paper I, and their physical resolution of 590×820 pc^2 in M51 would cover a 14×19 deg^2 area of the Perseus arm at a distance of 2.5 kpc; this is several times larger than the ~ 60 deg^2 integrated (ℓ, b) area of the CGPS Perseus HISA. Still, even if considerable cold H I is hidden in the spiral shock regions of M51, it is a separate question whether this H I is in mostly atomic or mostly molecular clouds; if the latter, the phase change picture remains open to question.

We will explore these issues in greater detail in a separate paper investigating the gas properties and degree of molecular association of the CGPS HISA (Gibson et al. 2005b).

5. Conclusions

In this paper, we have presented a comprehensive survey of H I self-absorption (HISA) features in the initial $73° \times 9°$ phase of the arcminute-resolution Canadian Galactic Plane Survey (CGPS). The CGPS HISA is a new tool for examining the detailed structure and distribution of cold H I clouds in a large area of the outer Galactic disk.

Using CLEAN-based spatial and spectral filter algorithms and full 3-D interpolation of the OFF-feature brightness to estimate the unabsorbed intensity along the feature sight line,

we extracted a set of HISA features that extend over the entire area of the survey where conditions allow detection, with sensitivity limits consistent with the noise and resolution properties of the H I data.

We compiled a catalog of contiguous, isolated features exceeding a minimum total absorption threshhold. A comparison of this catalog against prior HISA studies within the CGPS borders shows that we reproduce the majority of prior discoveries, with misses generally due to faint backgrounds occurring outside the range of our defined search parameters. At the same time, we identify a large number of new features not previously reported and image all HISA features in unprecedented detail. Small HISA structures can now be examined in the context of larger ones, and many trends in the general distribution become clear, such as the the concentration of strong HISA into a couple of very large complexes at Local velocities, and a similar concentration of strong HISA into a long series of complexes in the Perseus arm.

Statistically, the HISA detections fill a significant fraction of the searchable volume and suggest that the faintest HISA may be ubiquitous in the Galactic plane. This weak HISA "fluff" also appears to have little large-scale coherent structure in space or velocity but is as widespread as the available backgrounds allow. By contrast, strong HISA, which is much less abundant, is concentrated into larger, more discrete, and relatively solid structures.

Although the weak fluff and strong features occur within a continuum of amplitudes and other properties, we suggest they are made visible by two separate mechanisms. Physically, the weak fluff may be interpreted as a low-intensity population of small, slightly cool features scattered throughout the ambient ISM, which are produced and revealed by turbulent fluctuations in temperature and velocity. The strong HISA, on the other hand, requires significant density enhancements and/or very cold gas to produce its large absorption amplitudes, and it needs a large-scale background at the right velocity to absorb against in the outer Galaxy. We propose that the velocity reversal of the Perseus arm's spiral density wave provides the background for the strong HISA in this location, while the strength of the absorption is due to compression and cooling from the spiral shock. Spiral arms have long been thought to host the transformation of atomic gas into molecular clouds prior to forming new stars, but this has been very difficult to study in our own Galaxy. If HISA is revealing cold H I evolving into H_2 in a nearby spiral arm, this offers the exciting prospect of examining the molecular condensation process in great detail.

This paper is the second in an ongoing series investigating HISA at high resolution in the Galactic plane. A companion paper (Paper III) describes the HISA search and extraction algorithms at length, along with detailed evaluations of their reliability and completeness. A subsequent paper will analyze the CGPS HISA and CO distributions together and the gas

properties implied for the HISA by available constraints. A separate survey of the VGPS HISA in the inner Galaxy is also in preparation, as are extensions to the CGPS HISA survey coverage with new H I observations.

We thank W. McCutcheon, T. Landecker, and J. Stil for a number of useful discussions on this project, and the anonymous referee for constructive comments on the manuscript. W. Roberts graciously allowed the reproduction of the plots in Figure 9, T. Dame generously provided the CO survey data used in Figures 5 & 6 , and S. Strasser kindly made available the 21cm continuum maps used in Figure 2. We are very grateful to R. Gooch for tireless computing support, including continued expansion of the capabilities of the Karma visualization software package (Gooch 1996)[3], which was used extensively for this work. The Dominion Radio Astrophysical Observatory is operated as a national facility by the National Research Council of Canada. The Canadian Galactic Plane Survey (CGPS) is a Canadian project with international partners. The CGPS is described in Taylor et al. (2003)[4]. The main CGPS data set is available at the Canadian Astronomy Data Centre[5]. The CGPS is supported by a grant from the Natural Sciences and Engineering Research Council of Canada.

REFERENCES

Adler, D. S.; & Westpfahl, D. J. 1996, AJ, 111, 735

Baker, P. L., & Burton, W. B. 1979, A&AS, 35, 129

Bania, T. M., & Lockman, F. J. 1984, ApJS, 54, 513

Bergin, E. A., Hartmann, L. W., Raymond, J. C., & Ballesteros-Paredes, J. 2004, ApJ, 612, 921

Brogan, C. L., Zauderer, B. A., Lazio, T. J., Goss, W. M., De Pree, C. D., & Fasion, M. D. 2005, AJ, submitted

[3]See also http://www.atnf.csiro.au/karma.

[4]Additional information is available online at http://www.ras.ucalgary.ca/CGPS.

[5]See http://cadcwww.hia.nrc.ca/cgps.

Brunt, C. M., Kerton, C. R., Kothes, R., & Gibson, S. J. 2002, ASP Conf. Ser. 276, *Seeing Through the Dust: the Detection of H I and the Exploration of the ISM in Galaxies*, eds. A. R. Taylor, T. L. Landecker, & A. G. Willis, 140

Burton, W. B., Liszt, H. S., & Baker, P. L. 1978, ApJ, 219, L67

Chu, K. W. 1975, PhD Thesis, Caltech

Dame, T. M., Hartmann, D., & Thaddeus, P. 2001, ApJ, 547, 792

Dame, T. M., Ungerechts, H., Cohen, R. S., de Geus, E. J., Grenier, I. A., May, J., Murphy, D. C., Nyman, L.-A., & Thaddeus, P. 1987, ApJ, 322, 706

Dame, T. M., & Thaddeus, P. 1985, ApJ, 297, 751

Davies, R. D. 1956, MNRAS, 116, 443

Dewdney, P. E., & Roger, R. S. 1982, ApJ, 255, 564

Dickey, J. M., & Benson, J. M. 1982, AJ, 87, 278

Dickey, J. M., & Lockman, F. J. 1990, ARA&A, 28, 215

Dickey, J. M., McClure-Griffiths, N. M., Gaensler, B. M., & Green, A. J. 2003, ApJ, 585, 801

Feldt, C. 1993, A&A, 276, 531

Foster, T., Routledge, D., & Kothes, R. 2004, A&A, 417, 79

Frail, D. A., & Hjellming, R. M. 1991, AJ, 101, 2126

Garwood, R. W., & Dickey, J. M. 1989, ApJ, 338, 841

Gibson, S. J. 2002, ASP Conf. Ser. 276, *Seeing Through the Dust: the Detection of H I and the Exploration of the ISM in Galaxies*, eds. A. R. Taylor, T. L. Landecker, & A. G. Willis, 235

Gibson, S. J., Taylor, A. R., Dewdney, P. E., & Higgs, L. A. 2000, ApJ, 540, 851 (Paper I)

Gibson, S. J., Taylor, A. R., Dewney, P. E., Higgs, L. A., McCutcheon, W. H., & Wendker, H. J. 1999, ASP Conf. Ser. 168, *New Perspectives on the Interstellar Medium*, eds. A. R. Taylor, T. L. Landecker, & G. Joncas, 383

Gibson, S. J., Taylor, A. R., Brunt, C. M., Higgs, L. A., & Dewdney, P. E. 2005b, in preparation

Gibson, S. J., Taylor, A. R., Higgs, L. A., Brunt, C. M., & Dewdney, P. E. 2005a, ApJ, submitted (Paper III)

Gibson, S. J., Taylor, A. R., Stil, J. M., Higgs, L. A., Dewdney, P. E., & Brunt, C. M. 2004, in *How Does the Galaxy Work? A Galactic Tertulia with Don Cox and Ron Reynolds*, eds. E. J. Alfaro, E. Pérez, & J. Franco (Dordrecht: Kluwer Academic Publishers), 47

Gooch, R. 1996, ASP Conf. Ser. 101, *Astronomical Data Analysis Software and Systems V*, eds. G. H. Jacoby & J. Barnes, 80

Greisen, E. W. 1973, ApJ, 184, 363

Greisen, E. W., & Lockman, F. J. 1979, ApJ, 228, 740

Hartmann, D., & Burton, W. B. 1997, *Atlas of Galactic Neutral Hydrogen* (New York: Cambridge Univ. Press)

Hasegawa, T., Sato, F., & Fukui, Y. 1983, AJ, 88, 658

Henry, A. L., Quillen, A. C., & Gutermuth, R. 2004, AJ, 126, 2831

Heyer, M. H., & Terebey, S. 1998, ApJ, 502, 265

Higgs, L. A. 1999, ASP Conf. Ser. 168, *New Perspectives on the Interstellar Medium*, eds. A. R. Taylor, T. L. Landecker, & G. Joncas, 15

Higgs, L. A., & Tapping, K. F. 2000, AJ, 120, 2471

Higgs, L. A., Landecker, T. L., Asgekar, A., Davison, O. S., Rothwell, T. A., & Yar-Uyaniker, A. 2005, AJ, submitted

Högbom, J. A. 1974, A&AS, 15, 417

Höglund, B. & Andersson, C. 1974, A&A, 33, 389

Höglund, B. & Gordon, M. A. 1973, ApJ, 182, 45

Jenkins, E. B. 2004, Ap&SS, 289, 215

Kavars, D. W., Dickey, J. M., McClure-Griffiths, N. M., Gaensler, B. M., & Green, A. J. 2003, ApJ, 598, 1048

Keel, W. C., & White, R. E. 2001, AJ, 122, 1369

Khavtassi, J. Sh. 1960, *Atlas of Galactic Dark Nebulae*, Abastumani Astrophys. Obs. [Alternate spellings in ADS: Khavtasi, D. Sh.; Chavtasi, D. Sch.]

Knapp, G. R. 1974, AJ, 79, 527

Knee, L. B. G., & Brunt, C. M. 2001, Nature, 412, 308

Kothes, R., & Kerton, C. R. 2002, A&A, 390, 337

Kothes, R., Landecker, T. L., & Wolleben, M. 2004, ApJ, 607, 855

Koyama, H., & Inutsuka, S. 2002, ApJ, 564, L97

Koyama, H., & Inutsuka, S. 2000, ApJ, 532, 980

Kuchar, T. A., & Bania, T. M. 1994, ApJ, 436, 117

Kulkarni, S. R., & Heiles, C. 1988, in *Galactic and Extragalactic Radio Astronomy*, eds. G. L. Verschuur, & K. I. Kellermann (New York: Springer-Verlag), p. 95

Landecker, T. L., Roger, R. S., & Higgs, L. A. 1980, A&A, 39, 133

Lebrón, M., & Rodríguez, L. F. 1997, *Rev. Mex. Astron. Astrofis.*, 33, 165

Levinson, F. H., & Brown, R. L. 1980, ApJ, 242, 416

Li, D., & Goldsmith, P. F. 2003, ApJ, 585, 823

Lin, C. C., & Shu, F. H. 1964, ApJ, 140, 646

Lindblad, P. O. 1967, *Bull. Astr. Inst. Netherlands*, 19, 34

Lindblad, P. O., Grape, K., Sandqvist, A., & Schober, J. 1973, A&A, 24, 309

Lynds, B. T. 1962, ApJS, 7, 1

McClure-Griffiths, N. M., Dickey, J. M., Gaensler, B. M., Green, A. J., Haynes, R. F., & Wieringa, M. H. 2001a, PASA, 18, 84

McClure-Griffiths, N. M., Green, A. J., Dickey, J. M., Gaensler, B. M., Haynes, R. F., & Wieringa, M. H. 2001b, ApJ, 551, 394.

McCutcheon, W. H., Shuter, W. L. H., & Booth, R. S. 1978, MNRAS, 185, 755

Minn, Y. K. 1985, *J. Korean Ast. Soc.*, 18, 100

Minn, Y. K., & Greenberg, J. M. 1975, ApJ, 196, 161

Minn, Y. K., & Greenberg, J. M. 1973, *Ap. Lett.*, 13, 39

Minter, A. H., Lockman, F. J., Langston, G. I., & Lockman, J. A. 2001, ApJ, 555, 868

Montgomery, A. S., Bates, B., & Davies, R. D. 1995, MNRAS, 273, 449

Normandeau, M. 1999, AJ, 117, 2440

Olano, C. A. 2001, AJ, 121, 295

Peters, W. L., & Bash, F. N. 1987, ApJ, 317, 646

Plato 360 B.C., *The Republic*, VII, 514

Pringle, J. E., Allen, R. J., & Lubow, H. 2001, MNRAS, 327, 663

Quirk, W. J., & Crutcher, R. M. 1973, ApJ, 181, 359

Radhakrishnan, V. 1960, PASP, 72, 296

Radhakrishnan, V., Goss, W. M., Murray, J. D., & Brooks, J. W. 1972, ApJS, 24, 49

Read, P. L. 1981, MNRAS, 194, 863

Read, P. L. 1980, MNRAS, 192, 11

Reif, K., Booth, R., Mebold, U., & Winnberg, A. 1978, A&A, 70, 271

Roberts, W. W. 1993, PASP, 105, 670

Roberts, W. W. 1972, ApJ, 173, 259

Roberts, W. W. 1969, ApJ, 158, 123

Saito, T., Ohtani, H., & Tomita, Y. 1981, PASJ, 33, 327

Sánchez-Salcedo, F. J., Vázquez-Semadeni, E., & Gazol, A., 2002, ApJ, 577, 768

Sandqvist, Aa., Tomboulides, H., & Lindblad, P. O. 1988, A&A, 205, 225

Sato, F. 1990, AJ, 99, 1897

Sato, F., Whiteoak, J. B., Otrupcek, R. E., & Tokushige, T. 1992, AJ, 103, 1627

Schmidt, M. 1965, in *Stars and Stellar Systems V: Galactic Structure*, eds. A. Blaauw & M. Schmidt (Chicago: U. Chicago Press), 513

Schwarz, U. J., Goss, W. M., Kalberla, P. M., & Benaglia, P. 1995, A&A, 299, 193

Shu, F. H., Milione, V., Gebel, W., Yuan, C., Goldsmith, D. W., & Roberts, W. W. 1972, ApJ, 173, 557

Simonson, S. C., III, van Someren Greve, H. W. 1976, A&A, 49, 343

Sitnik, T. G., & Mel'Nik, A. M. 1999, *Astronomy Letters*, 25, 156

Snell, R. L. 1981, ApJS, 45, 121

Steer, D. G., Dewdney, P. E., & Ito, M. R. 1984, A&A, 137, 159

Strasser, S., & Taylor, A. R. 2004, ApJ, 603, 560

Taylor, A. R., et al. 2003, AJ, 125, 3145

Taylor, A. R., Stil, J. M., Dickey, J. M., McClure-Griffiths, N. M., Martin, P. G., Rothwell, T., & Lockman, F. J. 2002, ASP Conf. Ser. 276, *Seeing Through the Dust: the Detection of H I and the Exploration of the ISM in Galaxies*, eds. A. R. Taylor, T. L. Landecker, & A. G. Willis, 68

Tilanus, R. P. J., & Allen, R. J. 1991, A&A, 244, 8

van der Werf, P. P., Dewdney, P. E., Goss, W. M., & Vanden Bout, P. A. 1989, A&A, 216, 215

van der Werf, P. P., Goss, W. M., & Vanden Bout, P. A. 1988, A&A, 201, 311

Vogel, S. N., Kulkarni, S. R., & Scoville, N. Z. 1988, Nature, 334, 402

Wendker, H. J., Higgs, L. A., & Landecker, T. L. 1991, A&A, 241, 551

Wendker, H. J., Schramm, K. J., & Dieckvoss, C. 1983, A&A, 121, 69

Westerhout, G., & Wendlandt, H.-U. 1982, A&AS, 49, 143

Wild, J. P. 1952, ApJ, 115, 206

Willacy, K., Langer, W. D., & Allen, M. 2002, ApJ, 573, L119

Weaver, H., & Williams, D. R. W. 1973, A&AS, 8, 1

Wendker, H. J., & Wrigge, M. 1996, A&A, 305, 592

Wolfire, M. G., McKee, C. F., Hollenbach, D., & Tielens, A. G. G. M. 2003, ApJ, 587, 278

This preprint was prepared with the AAS LaTeX macros v5.2.

Table 1. Major CGPS HISA Features

Designation	ΔT-Weighted Position[a]			Coordinate Extent[b]			Volume[c]	Area[d]	$\int \Delta T dV$[e]	$\langle \Delta T \rangle$[f]	ΔT_{min}[g]	$\langle T_U \rangle$[h]	Diagnostics			Prior Detections[l]
	ℓ	b	v_{LSR}	$\Delta\ell$	Δb	Δv							ϕ_U[i]	η_V[j]	$\eta_{\Delta T}$[k]	
	deg	deg	km/s	deg	deg	km/s	deg^2 · km/s	deg^2	K deg^2 · km/s	K	K	K				Ref. ID
GHISA 079.88+0.62+02	79.882	+0.620	+2.13	11.075	7.710	26.38	54.407	16.671	−764.83	−14.06	−68.66	105.03	0.98	0.90	0.94	1,4,9,15,17,19,21,28
GHISA 083.87+1.74−74	83.866	+1.741	−74.41	0.480	0.370	8.24	0.160	0.064	−1.31	−8.20	−32.68	83.25	0.94	0.83	0.87	
GHISA 085.25+0.54−45	85.246	+0.543	−45.14	0.670	0.535	9.07	0.412	0.132	−5.86	−14.20	−37.96	85.77	0.91	0.90	0.92	
GHISA 085.85+0.95−41	85.852	+0.949	−40.67	0.395	0.290	6.60	0.117	0.051	−0.83	−7.13	−27.59	85.69	1.00	0.84	0.88	
GHISA 086.59+3.58−02	86.589	+3.576	−1.89	0.690	0.630	7.42	0.368	0.162	−3.69	−10.02	−38.12	101.37	1.00	0.80	0.84	
GHISA 086.71+2.41−04	86.710	+2.412	−4.25	0.325	0.205	9.07	0.111	0.037	−1.24	−11.21	−36.35	102.18	1.00	0.85	0.91	
GHISA 086.83+4.22−03	86.833	+4.216	−2.97	0.545	0.575	6.60	0.222	0.096	−2.05	−9.26	−31.74	100.68	1.00	0.79	0.83	
GHISA 088.09+4.72−02	88.089	+4.723	−2.21	0.430	0.260	8.24	0.108	0.054	−1.07	−9.89	−27.80	90.86	1.00	0.80	0.82	
GHISA 089.63+1.64−75	89.632	+1.639	−75.48	0.495	0.495	9.89	0.147	0.058	−1.32	−9.01	−29.69	79.61	0.52	0.78	0.82	
GHISA 089.96+2.79−91	89.963	+2.791	−90.77	0.240	0.180	7.42	0.120	0.031	−2.03	−16.87	−38.02	76.43	0.14	0.98	0.98	
GHISA 090.01+2.10−86	90.008	+2.095	−86.27	0.555	0.640	9.07	0.468	0.160	−7.83	−16.73	−40.83	73.14	0.01	0.95	0.96	
GHISA 090.35+3.04−87	90.352	+3.044	−86.77	0.405	0.410	9.07	0.152	0.066	−2.10	−13.82	−38.51	73.72	0.06	0.91	0.94	
GHISA 090.66+2.38−82	90.659	+2.379	−82.21	0.480	0.650	10.72	0.354	0.120	−5.07	−14.33	−41.60	79.36	0.44	0.93	0.96	
GHISA 091.39+1.91−82	91.390	+1.913	−81.77	0.330	0.430	9.89	0.197	0.053	−4.43	−22.54	−52.52	76.54	0.17	0.96	0.98	5
GHISA 091.63+2.00−72	91.629	+2.000	−71.87	0.365	0.315	9.89	0.139	0.050	−1.38	−9.87	−32.23	91.04	1.00	0.83	0.86	
GHISA 091.90+3.27−03	91.898	+3.275	−3.21	6.105	3.625	22.26	25.058	7.543	−601.78	−24.02	−80.72	88.20	0.74	0.95	0.98	1,4,7,8,13,25,28
GHISA 092.41+0.92−01	92.411	+0.923	−1.20	0.400	0.465	9.07	0.162	0.063	−1.73	−10.65	−37.26	99.06	1.00	0.83	0.87	
GHISA 093.85+0.41−01	93.853	+0.412	−0.55	0.990	1.435	11.54	0.504	0.247	−5.37	−10.65	−40.31	86.66	0.90	0.80	0.84	
GHISA 094.32−0.10−43	94.322	−0.098	−43.27	3.205	2.260	18.96	3.263	1.274	−33.18	−10.17	−40.01	85.56	0.79	0.84	0.88	5
GHISA 094.42+1.21−58	94.422	+1.214	−57.69	0.405	0.365	9.89	0.113	0.039	−1.94	−17.16	−36.56	77.74	0.23	0.88	0.90	
GHISA 095.39+1.06−64	95.391	+1.057	−63.72	0.360	0.240	7.42	0.132	0.042	−1.38	−10.43	−34.06	84.43	1.00	0.92	0.94	
GHISA 096.40−0.61−40	96.401	−0.606	−40.23	0.585	0.390	9.07	0.181	0.069	−2.40	−13.23	−34.30	82.92	0.73	0.91	0.92	
GHISA 097.16+1.76−65	97.159	+1.760	−65.17	0.800	0.655	9.89	0.306	0.139	−2.77	−9.06	−32.29	91.78	1.00	0.76	0.80	
GHISA 098.69+0.70−13	98.685	+0.704	−12.94	1.335	1.385	9.07	1.209	0.543	−14.59	−12.07	−37.90	77.74	0.22	0.86	0.88	
GHISA 104.11+1.15−54	104.112	+1.151	−54.11	0.395	0.375	9.07	0.188	0.065	−2.18	−11.61	−33.54	90.75	0.99	0.87	0.90	
GHISA 104.44+0.52−54	104.435	+0.516	−53.86	1.885	1.005	18.14	1.464	0.538	−15.27	−10.44	−44.31	87.42	0.82	0.83	0.87	
GHISA 106.53+0.93−59	106.533	+0.934	−58.91	0.390	0.400	14.02	0.241	0.085	−2.28	−9.45	−31.56	73.54	0.00	0.88	0.90	
GHISA 107.45+0.21−51	107.449	+0.213	−50.61	0.605	0.385	7.42	0.309	0.105	−3.68	−11.94	−48.71	95.81	1.00	0.89	0.93	5
GHISA 109.42−1.32−48	109.425	−1.322	−47.82	0.625	0.955	10.72	0.443	0.194	−3.74	−8.45	−27.50	78.32	0.15	0.84	0.88	
GHISA 110.27−0.33−51	110.268	−0.329	−51.39	0.560	0.525	9.89	0.287	0.113	−3.48	−12.12	−41.32	76.02	0.18	0.85	0.89	3
GHISA 113.13−0.98−37	113.128	−0.985	−36.62	0.425	0.225	5.77	0.132	0.063	−1.46	−11.00	−31.59	77.78	0.32	0.92	0.94	
GHISA 113.34+1.01−11	113.336	+1.013	−11.16	0.680	0.420	9.07	0.285	0.111	−2.93	−10.28	−33.48	73.05	0.00	0.87	0.90	

Table 1—Continued

Designation	ΔT-Weighted Position[a]			Coordinate Extent[b]			Volume[c]	Area[d]	$\int \Delta T dV$[e]	$\langle \Delta T \rangle$[f]	ΔT_{min}[g]	$\langle T_U \rangle$[h]	Diagnostics			Prior Detections[l]
	ℓ	b	v_{LSR}	$\Delta\ell$	Δb	Δv							ϕ_U[i]	η_V[j]	$\eta_{\Delta T}$[k]	
	deg	deg	km/s	deg	deg	km/s	deg^2 · km/s	deg^2	K deg^2 · km/s	K	K	K				Ref. ID
GHISA 114.48+2.18−13	114.481	+2.180	−12.66	0.755	0.355	4.12	0.103	0.068	−1.38	−13.40	−30.61	72.40	0.00	0.78	0.81	
GHISA 115.39−1.67−43	115.394	−1.674	−42.89	0.550	0.305	7.42	0.180	0.075	−2.43	−13.53	−39.03	75.10	0.15	0.88	0.92	
GHISA 116.36−2.02−45	116.364	−2.017	−45.30	0.445	0.225	6.60	0.105	0.040	−1.27	−12.07	−29.60	73.03	0.00	0.88	0.91	
GHISA 118.69+2.60−64	118.691	+2.598	−64.04	0.380	0.275	7.42	0.131	0.052	−1.89	−14.40	−34.30	71.79	0.00	0.92	0.94	
GHISA 119.34−1.56−35	119.344	−1.561	−35.18	0.735	0.880	8.24	0.629	0.261	−6.81	−10.83	−40.41	73.64	0.01	0.88	0.92	5
GHISA 120.80+0.60−51	120.804	+0.603	−51.23	0.895	1.100	9.07	0.925	0.332	−11.78	−12.73	−47.33	82.30	0.71	0.88	0.93	
GHISA 120.87−0.70−43	120.874	−0.699	−42.98	0.660	0.505	8.24	0.316	0.128	−3.85	−12.20	−40.56	75.12	0.05	0.91	0.95	
GHISA 121.14−0.19−52	121.141	−0.187	−51.96	0.410	0.250	6.60	0.114	0.048	−1.30	−11.37	−30.79	72.55	0.00	0.86	0.90	
GHISA 122.84+1.80−57	122.843	+1.800	−56.59	1.025	0.390	9.07	0.248	0.122	−2.72	−10.97	−36.35	82.03	0.73	0.80	0.84	
GHISA 122.87+2.24−60	122.870	+2.238	−59.57	0.840	0.410	9.07	0.358	0.133	−4.51	−12.57	−38.91	89.87	1.00	0.90	0.92	
GHISA 124.71+0.29−44	124.706	+0.294	−43.93	0.420	0.595	9.07	0.244	0.087	−2.71	−11.11	−37.41	80.11	0.49	0.87	0.91	
GHISA 124.81+1.04−57	124.810	+1.045	−56.94	0.510	0.385	8.24	0.186	0.072	−1.71	−9.23	−33.63	78.87	0.36	0.85	0.89	
GHISA 126.68+0.76−55	126.682	+0.759	−54.52	0.395	0.285	6.60	0.104	0.050	−1.13	−10.84	−30.70	71.70	0.00	0.81	0.84	
GHISA 126.89+1.61−58	126.887	+1.613	−57.75	0.345	0.395	9.07	0.217	0.081	−2.75	−12.66	−41.63	74.68	0.00	0.90	0.93	
GHISA 127.72+0.94−55	127.716	+0.941	−54.90	0.450	0.320	7.42	0.105	0.049	−1.02	−9.66	−33.23	92.38	1.00	0.75	0.78	
GHISA 127.86−0.31−43	127.859	−0.312	−43.28	0.355	0.440	4.95	0.112	0.055	−0.95	−8.46	−27.65	71.63	0.00	0.80	0.84	
GHISA 128.15+0.21−44	128.152	+0.207	−44.37	0.385	0.215	10.72	0.108	0.038	−1.49	−13.86	−38.18	78.79	0.35	0.87	0.89	
GHISA 128.35+0.01−44	128.349	+0.009	−44.28	0.385	0.180	13.19	0.123	0.036	−1.95	−15.94	−47.30	73.82	0.00	0.89	0.91	
GHISA 129.50+0.97−49	129.499	+0.973	−49.16	0.675	0.975	7.42	0.335	0.147	−3.33	−9.94	−43.52	89.73	0.99	0.78	0.82	
GHISA 130.37+1.30−46	130.365	+1.300	−46.15	0.720	0.425	5.77	0.125	0.070	−1.02	−8.10	−30.88	77.70	0.06	0.68	0.71	
GHISA 133.71−0.03−49	133.714	−0.032	−48.63	4.790	3.145	23.91	10.778	3.505	−166.85	−15.48	−57.40	89.89	0.87	0.90	0.93	5,12,14,18
GHISA 136.42+0.02−36	136.422	+0.016	−36.50	0.505	0.345	7.42	0.152	0.066	−1.53	−10.04	−33.66	83.43	0.89	0.82	0.85	
GHISA 136.83+0.92−38	136.830	+0.923	−37.73	0.990	0.920	11.54	0.571	0.251	−5.33	−9.33	−34.00	74.51	0.01	0.82	0.85	18
GHISA 137.88−0.70−40	137.880	−0.703	−39.96	0.390	0.325	8.24	0.121	0.044	−1.24	−10.25	−39.37	98.89	1.00	0.85	0.90	
GHISA 137.95−0.27−37	137.954	−0.265	−36.92	0.610	0.415	6.60	0.129	0.070	−0.99	−7.69	−34.67	100.50	1.00	0.65	0.69	
GHISA 139.01+0.96−40	139.007	+0.964	−40.32	2.245	1.685	12.37	3.591	1.292	−45.93	−12.79	−44.13	91.52	0.99	0.89	0.92	5,18,22,23,24
GHISA 139.21−0.60−40	139.207	−0.597	−40.13	0.765	1.050	9.07	0.691	0.278	−7.93	−11.49	−42.82	99.91	1.00	0.86	0.90	24
GHISA 140.55+0.49−45	140.550	+0.495	−44.79	0.965	0.930	9.07	0.396	0.207	−4.47	−11.28	−33.17	94.07	1.00	0.83	0.85	18,24
GHISA 140.72+1.48−40	140.722	+1.478	−40.30	0.655	0.755	8.24	0.275	0.116	−2.92	−10.62	−38.27	92.51	1.00	0.80	0.83	22
GHISA 141.10−0.60−41	141.100	−0.604	−40.63	1.455	1.035	11.54	1.317	0.514	−15.89	−12.06	−47.18	103.22	1.00	0.87	0.91	24
GHISA 141.37−1.70−41	141.366	−1.698	−41.01	0.290	0.420	5.77	0.139	0.062	−1.26	−9.07	−29.24	87.02	0.99	0.80	0.83	
GHISA 141.62+0.60−42	141.623	+0.603	−41.82	0.595	0.320	5.77	0.107	0.059	−0.91	−8.55	−36.71	102.46	1.00	0.64	0.68	24

Table 1—Continued

Designation	ΔT-Weighted Position[a]			Coordinate Extent[b]			Volume[c]	Area[d]	$\int \Delta T dV$[e]	$\langle \Delta T \rangle$[f]	ΔT_{min}[g]	$\langle T_U \rangle$[h]	Diagnostics			Prior Detections[l]
	ℓ	b	v_{LSR}	$\Delta\ell$	Δb	Δv							ϕ_U[i]	η_V[j]	$\eta_{\Delta T}$[k]	
	deg	deg	km/s	deg	deg	km/s	deg^2 · km/s	deg^2	K deg^2 · km/s	K	K	K				Ref. ID
GHISA 142.61−0.18−41	142.607	−0.179	−41.41	0.750	1.070	7.42	0.452	0.228	−4.00	−8.86	−36.87	107.54	1.00	0.73	0.77	
GHISA 144.07+0.72−33	144.066	+0.717	−33.13	0.565	0.420	9.89	0.166	0.077	−1.61	−9.71	−30.79	83.99	0.89	0.83	0.86	
GHISA 144.52−1.23−31	144.523	−1.227	−30.73	0.645	0.755	9.89	0.507	0.204	−8.72	−17.19	−51.57	92.53	1.00	0.87	0.91	
GHISA 145.01+0.46−35	145.013	+0.460	−34.68	0.910	1.610	14.84	0.993	0.353	−14.88	−14.98	−54.69	89.14	0.86	0.87	0.91	
GHISA 145.81+0.96−36	145.813	+0.958	−36.12	0.750	0.485	9.07	0.266	0.106	−2.94	−11.05	−43.67	84.15	0.91	0.83	0.88	

[a]Average feature coordinates, weighted by ΔT

[b]Dimensions of the (ℓ, b, v) box containing the feature

[c]Volume occupied by $|\Delta T| > 0$ voxels

[d]Projected area of feature volume

[e]3-D integrated absorption of feature

[f]Mean absorption per voxel

[g]Maximum absorption in any voxel ($\Delta T_{min} = -|\Delta T|_{max}$)

[h]Mean T_U per voxel

[i]Fraction of detected volume for which $T_U \geq 80$ K and detections are most complete, based on f_{det}

[j]Fraction of detected volume that is probably reliable, based on $f_{true}(\ell, b, v)$

[k]Fraction of detected 3-D integrated absorption that is probably reliable, based on $f_{true}(\ell, b, v)$

[l]Prior detections of this feature in the literature, if any; see Table 2 for reference notes

Table 2. Prior HISA Studies in the CGPS Region

Ref. ID	Reference	Telescope	Beam[a] deg	Δv[b] km/s	Map[c]	Number of features covered[d]	found[e]	major[f]
1	Davies (1956)	Jodrell Bank 9m	1.6	4.2	n	4	3	2
2	Minn & Greenberg (1973)	Green Bank 91m[g]	0.22	1.0	n	1	1	0
3	Höglund & Gordon (1973)	Green Bank 91m[g]	0.22	1.0	Y	1	1	1
4	Knapp (1974)	Green Bank 43m	0.35	0.08-0.34	n	4	3	2
5	Höglund & Andersson (1974)	Green Bank 91m[g]	0.22	1.0	n	41	29	17
6	Minn & Greenberg (1975)	Green Bank 91m[g]	0.22	1.0	Y	1	1	0
7	Simonson & van Someren Greve (1976)	Dwingeloo 25m	0.60	1.7	Y	1	1	1
8	Reif et al. (1978)	Bonn 100m	0.15	0.21	n	1	1	1
9	Landecker et al. (1980)	DRAO ST + 26m	0.05	1.6	Y	1	1	1
10	Read (1980)	Cambridge Half-Mile	0.03	3.3	Y	4	2	0
11	Snell (1981)	Green Bank 43m	0.35	0.69	n	1	0	0
12	Read (1981)	Cambridge Half-Mile	0.03	3.3	Y	4	4	4
13	Saito et al. (1981)	Hat Creek 26m[h]	0.59	1.1	Y	1	1	1
14	Hasegawa et al. (1983)	Green Bank 91m[g]	0.22	1.0	Y	6	6	6
15	Wendker et al. (1983)	Bonn 100m	0.15	0.8	Y	1	1	1
16	Minn (1985)	Green Bank 91m[g]	0.22	1.0	n	3	1	0
17	Sandqvist et al. (1988)	Green Bank 91m	0.17	0.69	n	3	2	1
18	Sato (1990)	Green Bank 91m[g]	0.22	1.0	Y	13	10	8
19	Feldt (1993)	DRAO ST + Bonn 100m	0.03	1.3	Y	7	4	4
20	Schwarz et al. (1995)	WSRT + Bonn 100m	0.02	0.52	Y	1	1	0
21	Wendker & Wrigge (1996)	DRAO ST + Bonn 100m	0.03	1.3	n	1	1	1
22	Higgs (1999)	DRAO ST + 26m[i]	0.02	0.82	Y	3	3	3
23	Gibson et al. (1999)	DRAO ST + 26m[i]	0.02	0.82	Y	2	1	1
24	Gibson et al. (2000)	DRAO ST + 26m[i]	0.02	0.82	Y	3	3	2
25	Higgs & Tapping (2000)	DRAO 26m	0.62	0.82	Y	1	1	1
26	Knee & Brunt (2001)	DRAO ST + 26m[i]	0.02	0.82	Y	1	0	0
27	Foster et al. (2004)	DRAO ST + 26m[i]	0.02	0.82	Y	1	1	0
28	Higgs et al. (2005)	DRAO 26m	0.62	0.82	Y	3	3	3

[a]Angular resolution (FWHM)

[b]Velocity channel separation

[c]Were maps made of HISA features?

[d]Features within the CGPS Phase I coverage

[e]Features detected wholly or partially in this HISA search (e.g., in Figure 1)

[f]Features overlapping with major features in this survey (see Table 1)

[g]Maryland-Green Bank Galactic 21cm Line Survey data (Westerhout & Wendlandt 1982)

[h]Berkeley Low-Latitude Survey of Neutral Hydrogen data (Weaver & Williams 1973)

[i]Canadian Galactic Plane Survey data (Taylor et al. 2003)

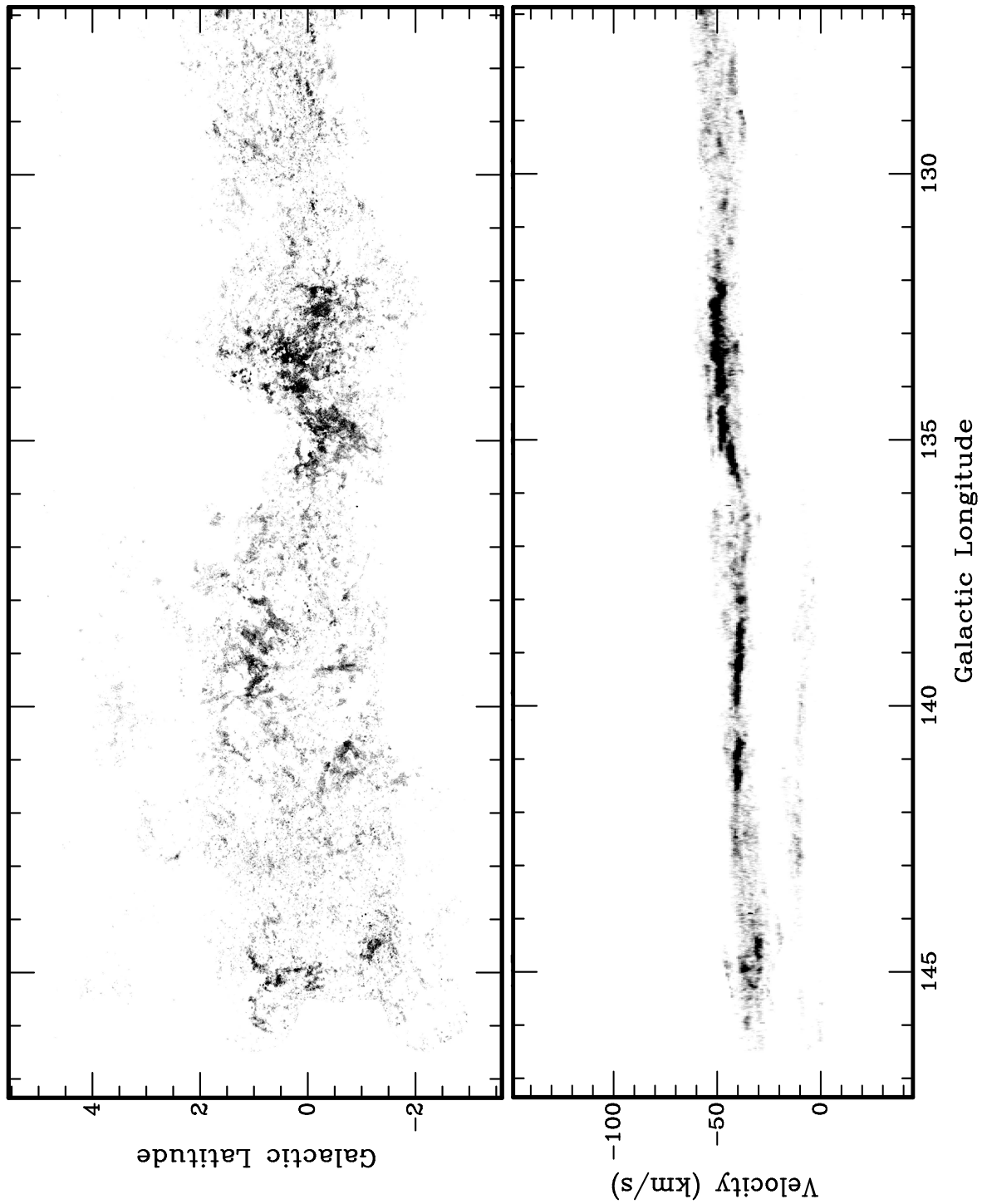

Fig. 1.— *(a)* Detected HISA in the CGPS over the longitude range $127° \leq \ell \leq 147°$, showing the amplitude ΔT in (ℓ, b) integrated over v and in (ℓ, v) integrated over b. Intensity ranges are -82.446 to 0 $\mathrm{K\,km\,s^{-1}}$ and -5.0 to 0 $\mathrm{K\,deg}$, respectively. *(b-d)* Same as *(a)*, except covering $109° \leq \ell \leq 130°$, $92° \leq \ell \leq 112°$, and $74° \leq \ell \leq 94°$, respectively. The longitude ranges match those shown in Figure 7 of Taylor et al. (2003).

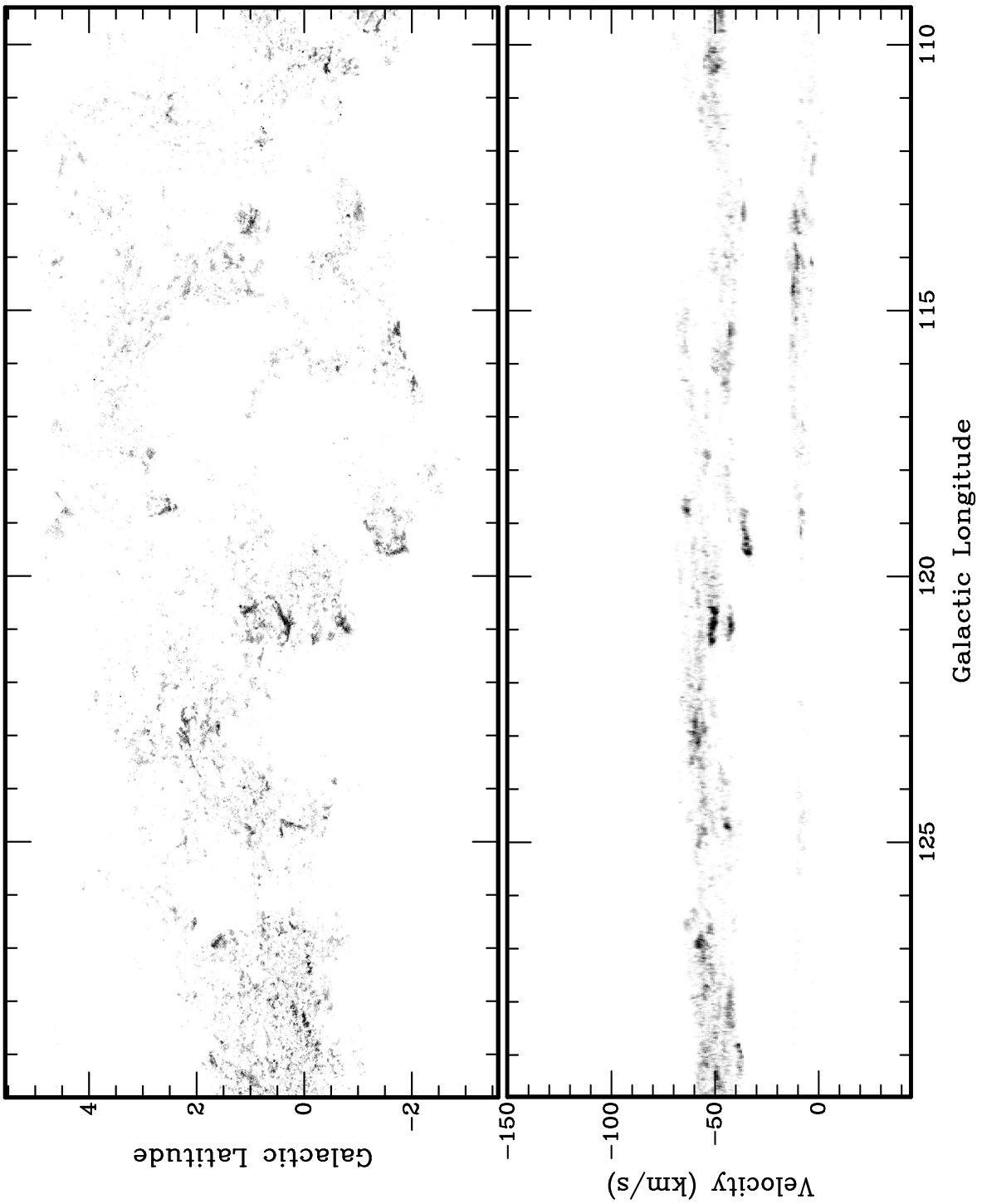

Fig. 1b.— (ℓ, b) and (ℓ, v) maps of HISA ΔT, continued.

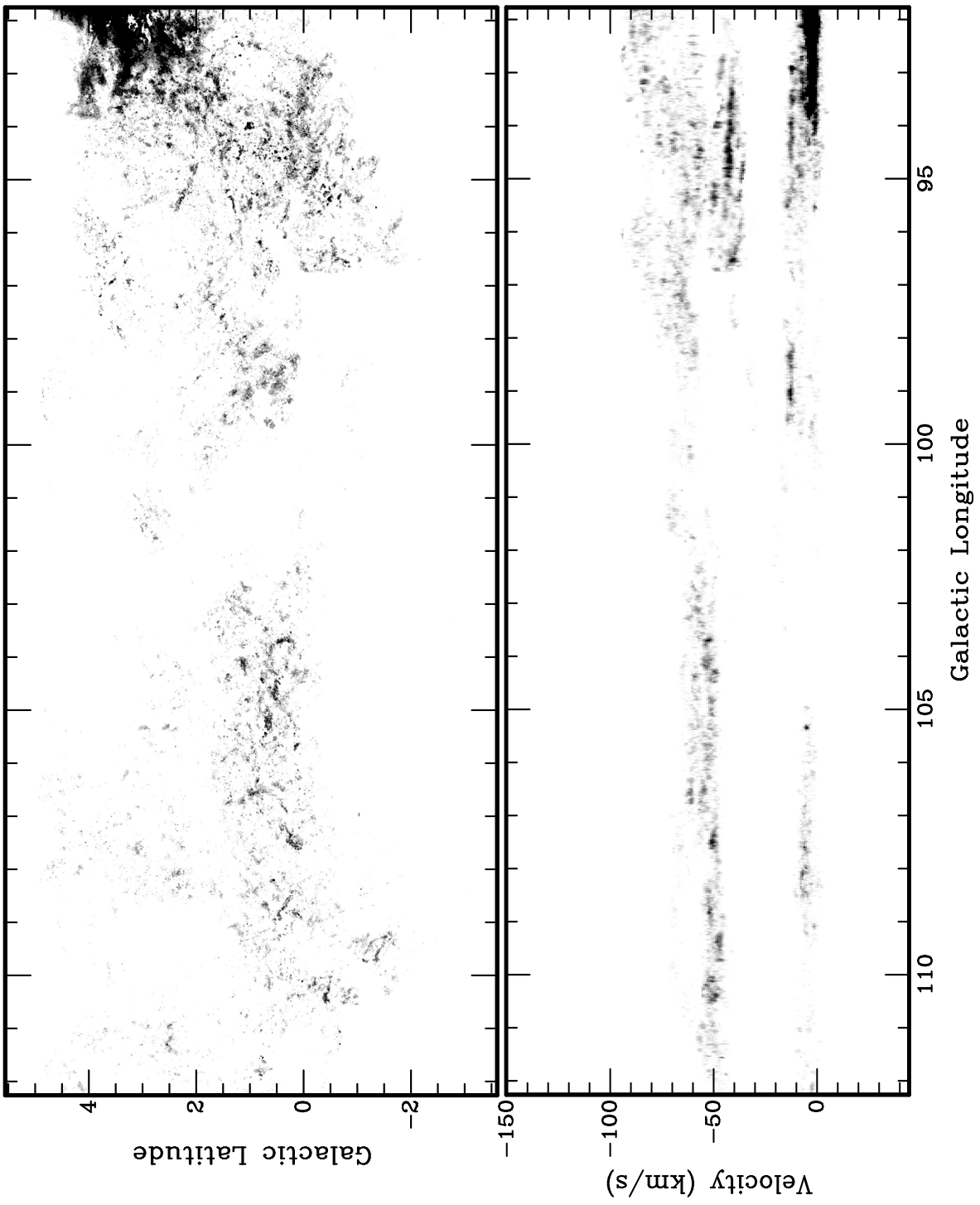

Fig. 1c.— (ℓ, b) and (ℓ, v) maps of HISA ΔT, continued.

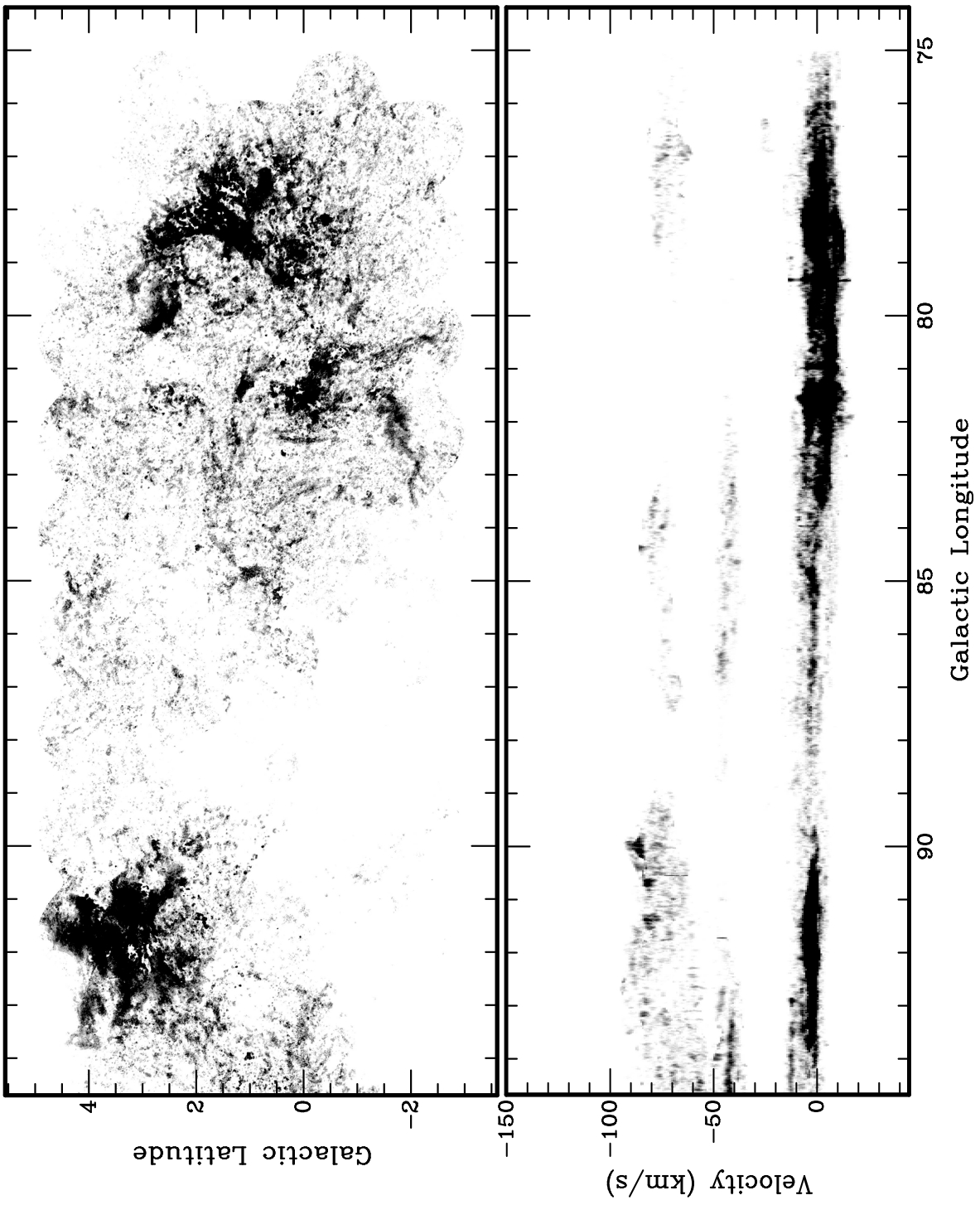

Fig. 1d.— (ℓ, b) and (ℓ, v) maps of HISA ΔT, continued.

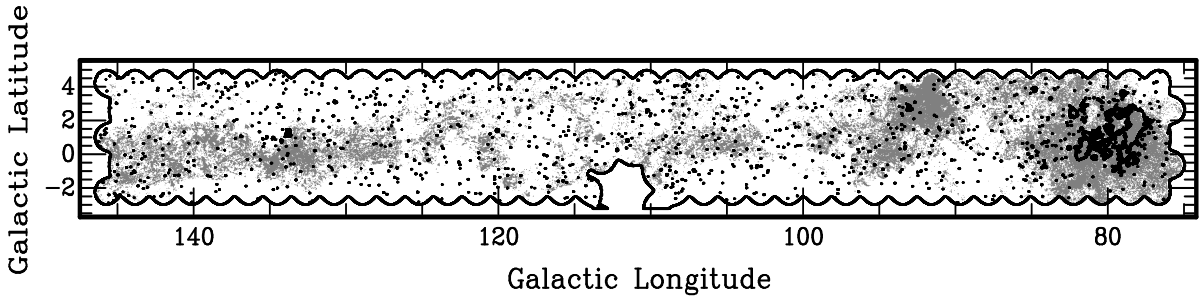

Fig. 2.— Limits on HISA detection from 20′ mosaic edge clipping, synthesis field weight clipping, and possible contamination from 21cm continuum emission. The background image shows all HISA detections over the (ℓ, b) area of the survey (see Fig. 1 for a more detailed view). Contours around the periphery indicate the boundaries set by the two clipping requirements. Additional contours scattered throughout the interior of the survey outline regions where the continuum brightness T_C is $\geq$ 20 K, using matching-beam continuum maps provided by S. Strasser. See text for discussion.

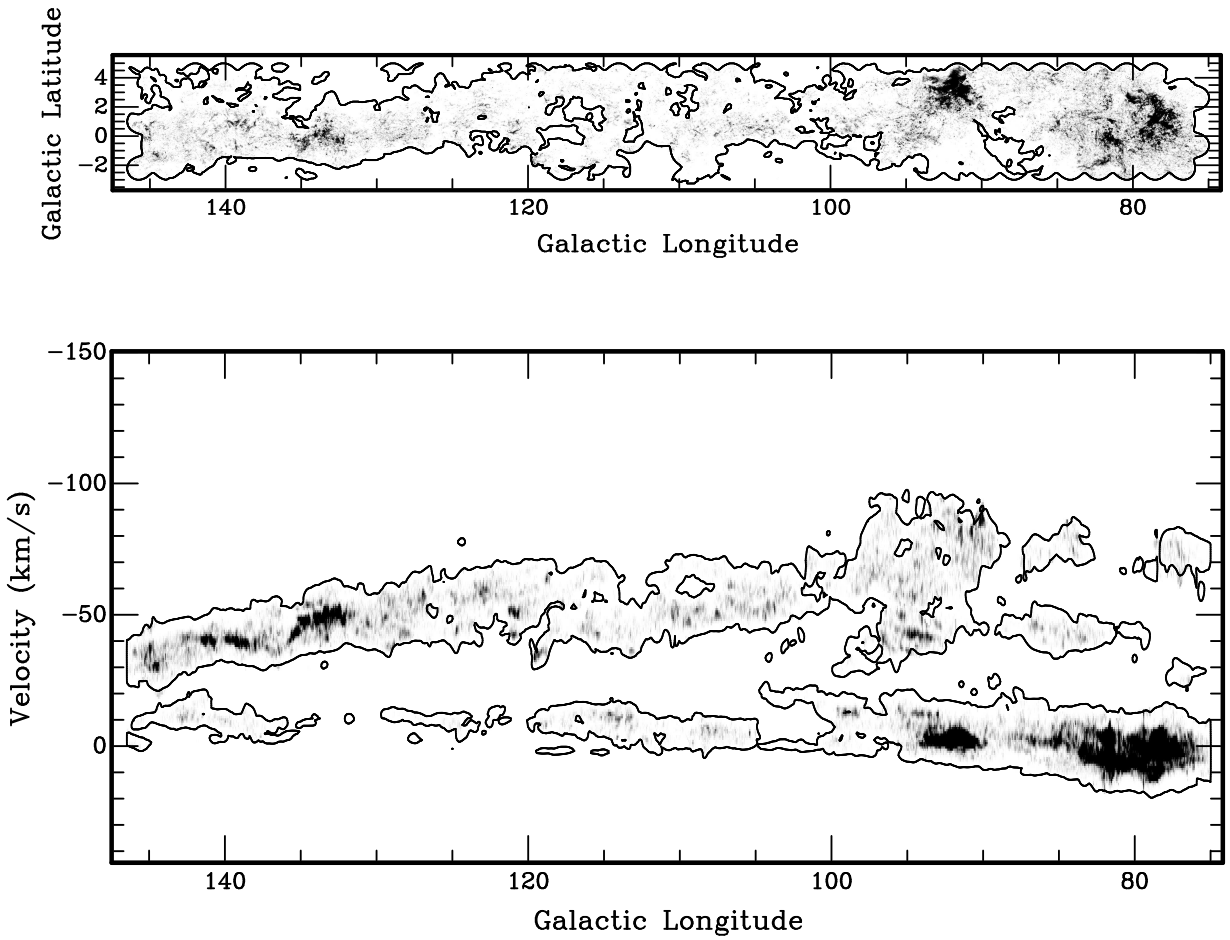

Fig. 3.— Detected HISA ΔT (background image) in (ℓ, b) and (ℓ, v), with the same intensity ranges used in Figure 1. Contours show the approximate detection boundaries imposed by requiring $T_U \geq 70$ K in addition to the peripheral limits shown in Figure 2; these boundaries represent the "searchable area" of the survey. See text for further details.

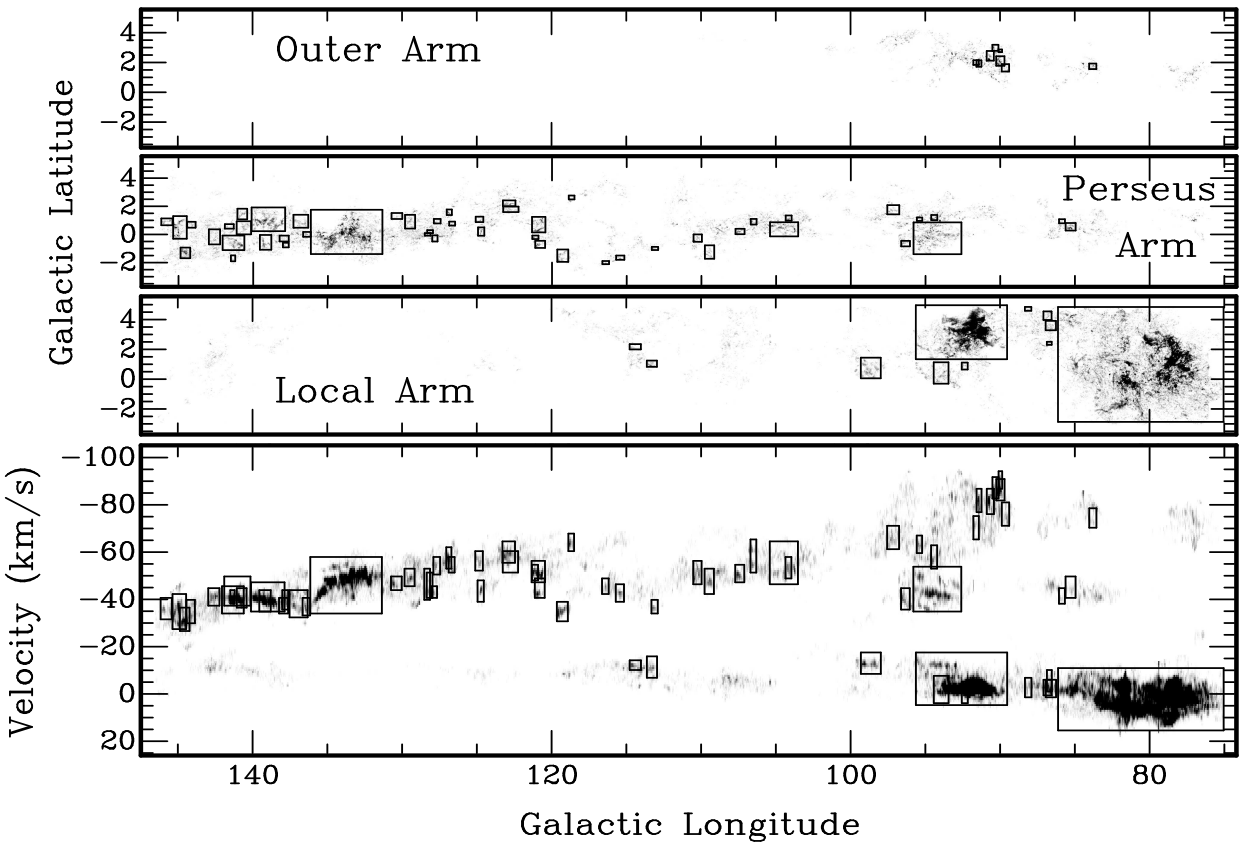

Fig. 4.— Detected HISA ΔT as shown in Figures 1 & 3, but with the (ℓ, b) projections over the velocity subranges $v_{LSR} < -70\,\mathrm{km\,s^{-1}}$, $-20\,\mathrm{km\,s^{-1}} < v_{LSR} - 70\,\mathrm{km\,s^{-1}}$, and $v_{LSR} > -20\,\mathrm{km\,s^{-1}}$, corresponding to the Outer, Perseus, and Local spiral arms, respectively. Boxes mark the (ℓ, b, v) extents of features catalogued in Table 1.

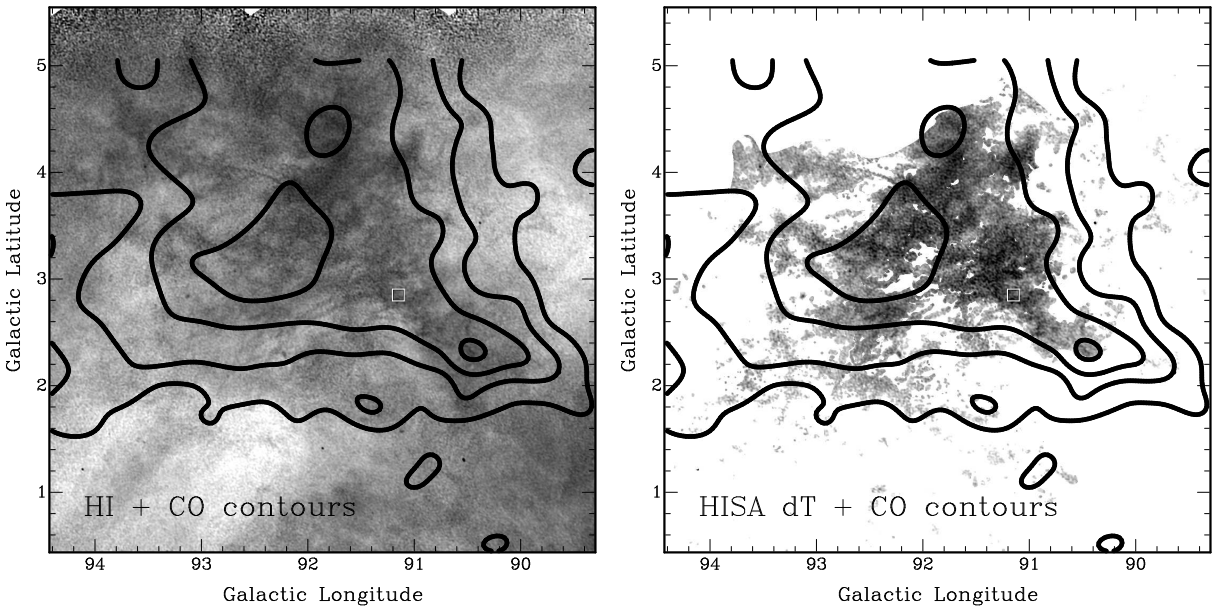

Fig. 5.— (ℓ, b) channel maps of the central concentration of feature GHISA 091.90+3.27−03 at -3 km s^{-1}. Shown are H I brightness and HISA ΔT, with ^{12}CO $J = 1 - 0$ emission from Dame et al. (2001) at contour levels of 1, 2, 3, and 4 K. Intensity ranges are 0 to +130 K for the H I panel and −65 to 0 K for the ΔT panel. The small white $6' \times 6'$ box ($\ell = 91.15°, b = +2.85°$) marks the area from which the spectra in Figure 6 were taken. The feature extraction is truncated for $b \gtrsim +4.5°$ due to $T_U < 70$ K (see §3.1 and Fig. 3).

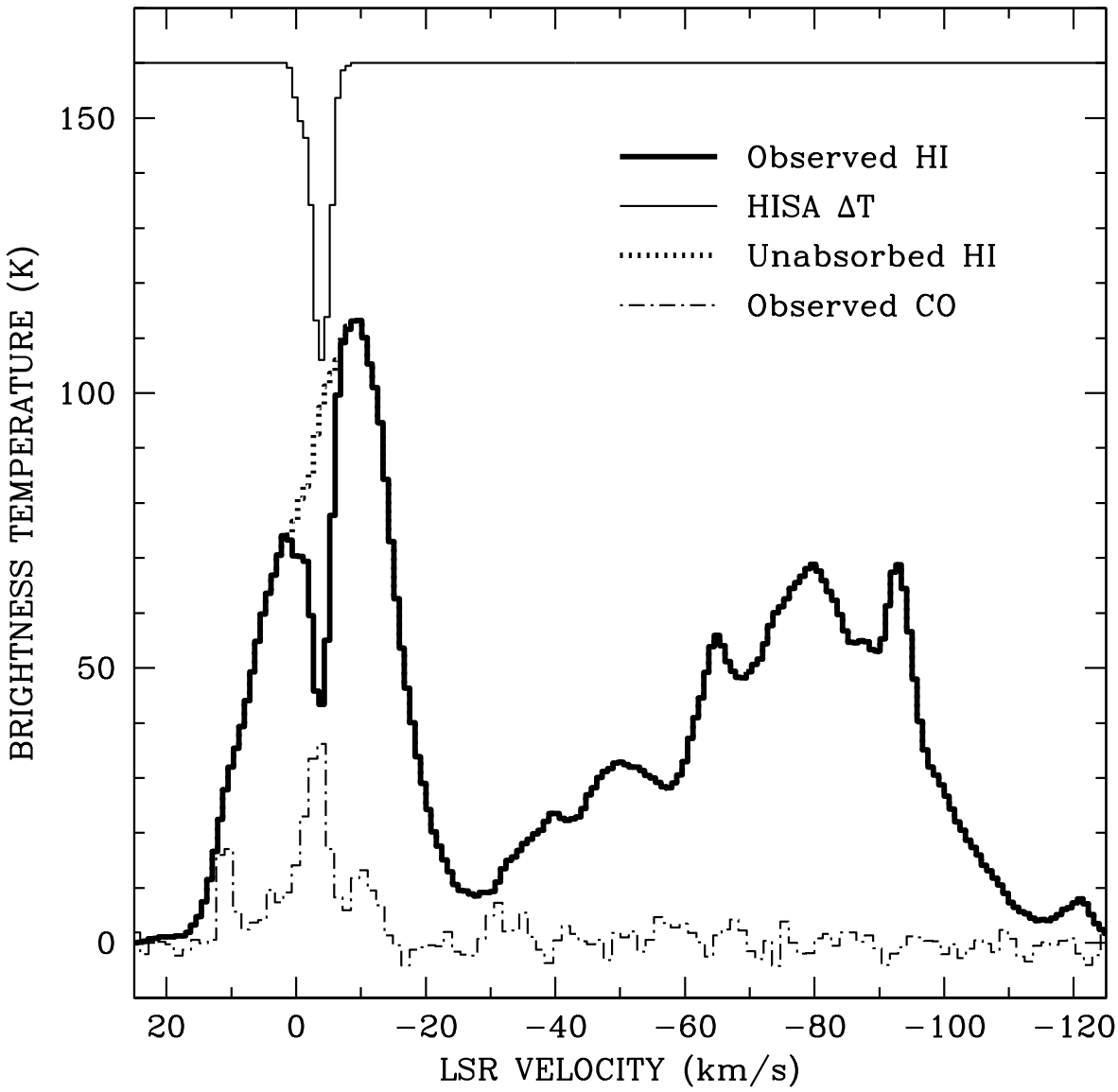

Fig. 6.— Spatially-averaged velocity spectra extracted from the $6' \times 6'$ box marked in Figure 5 at $(\ell = 91.15°, b = +2.85°)$. Shown are H I emission, HISA ΔT, and ^{12}CO $J = 1-0$ emission from Dame et al. (2001). For clarity, the ΔT zero-point has been shifted to 160 K, and the CO brightness has been multiplied by 10.

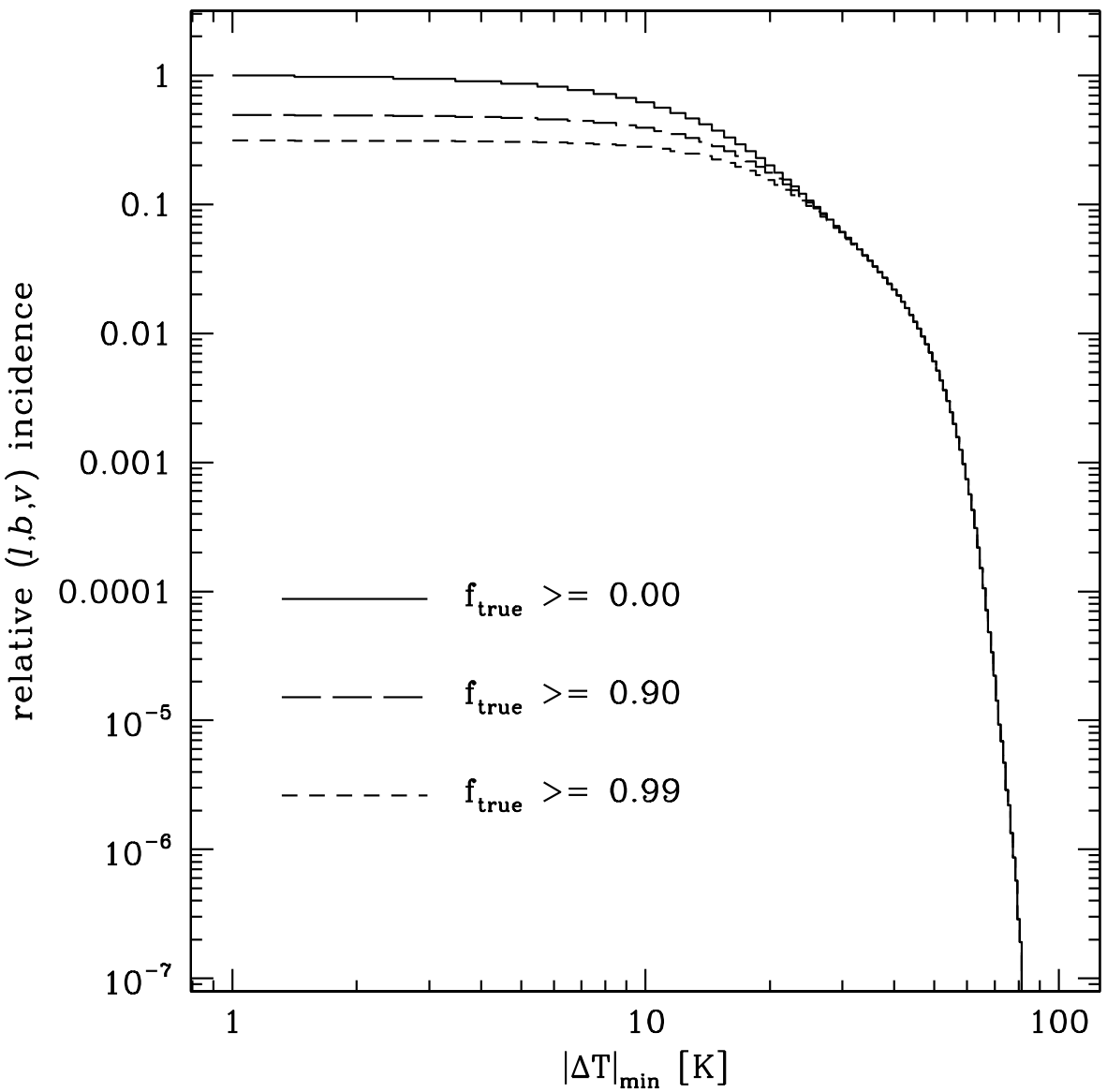

Fig. 7.— The relative incidence of HISA voxels in the CGPS for a minimum $|\Delta T|$ and a minimum f_{true}. 49% of all voxels have at least 90% reliability, and 31% have at least 99% reliability. This cumulative plot peaks at $|\Delta T|_{min} \rightarrow 0$, but few voxels are this faint; the ΔT distribution itself peaks at ~ -10 K (see Paper III, Fig. 11).

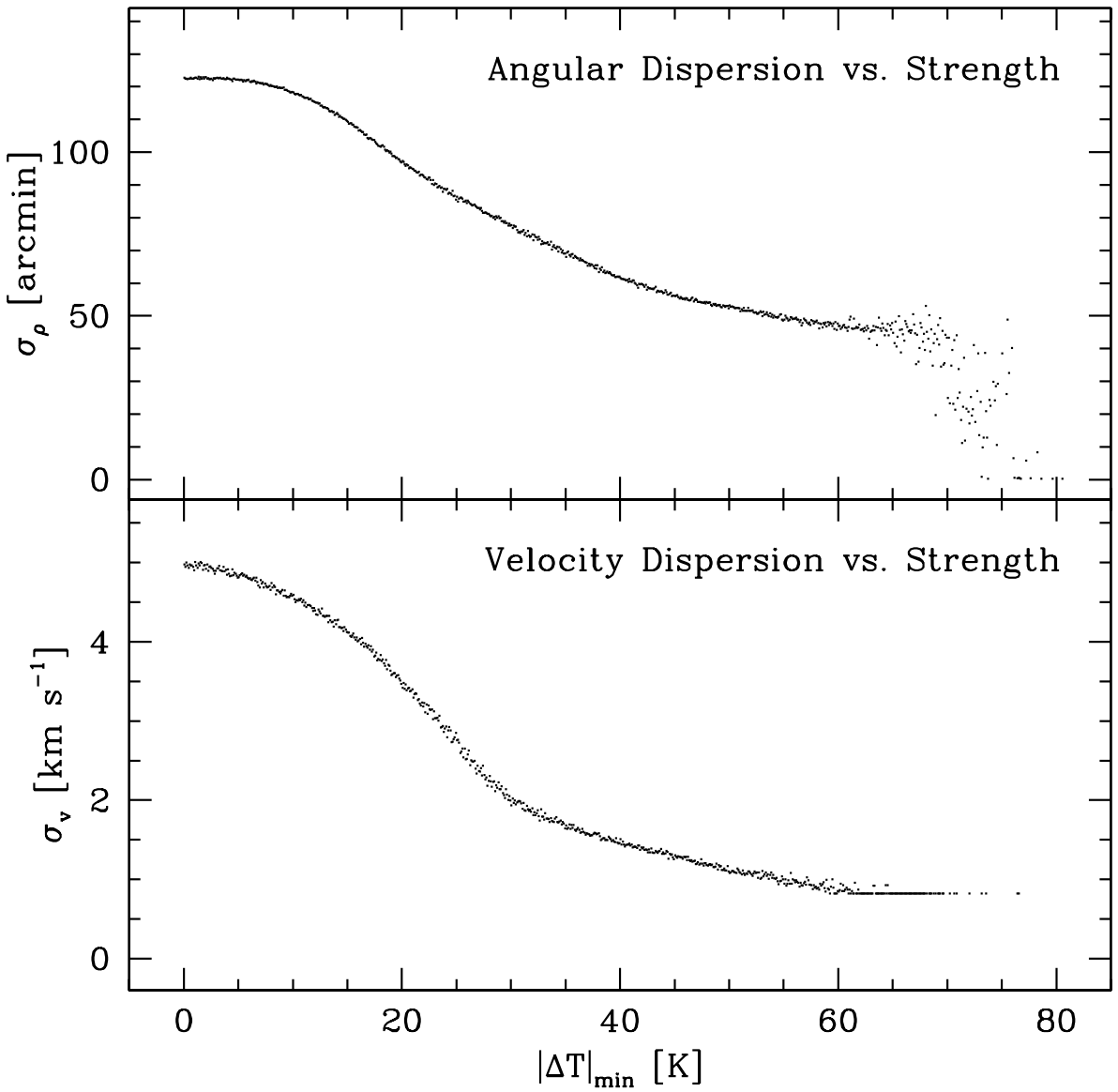

Fig. 8.— The dispersion of HISA voxel pairs in angle and velocity for HISA with $|\Delta T| \geq |\Delta T|_{min}$ in both voxels. Large-amplitude HISA is relatively more concentrated than small-amplitude HISA.

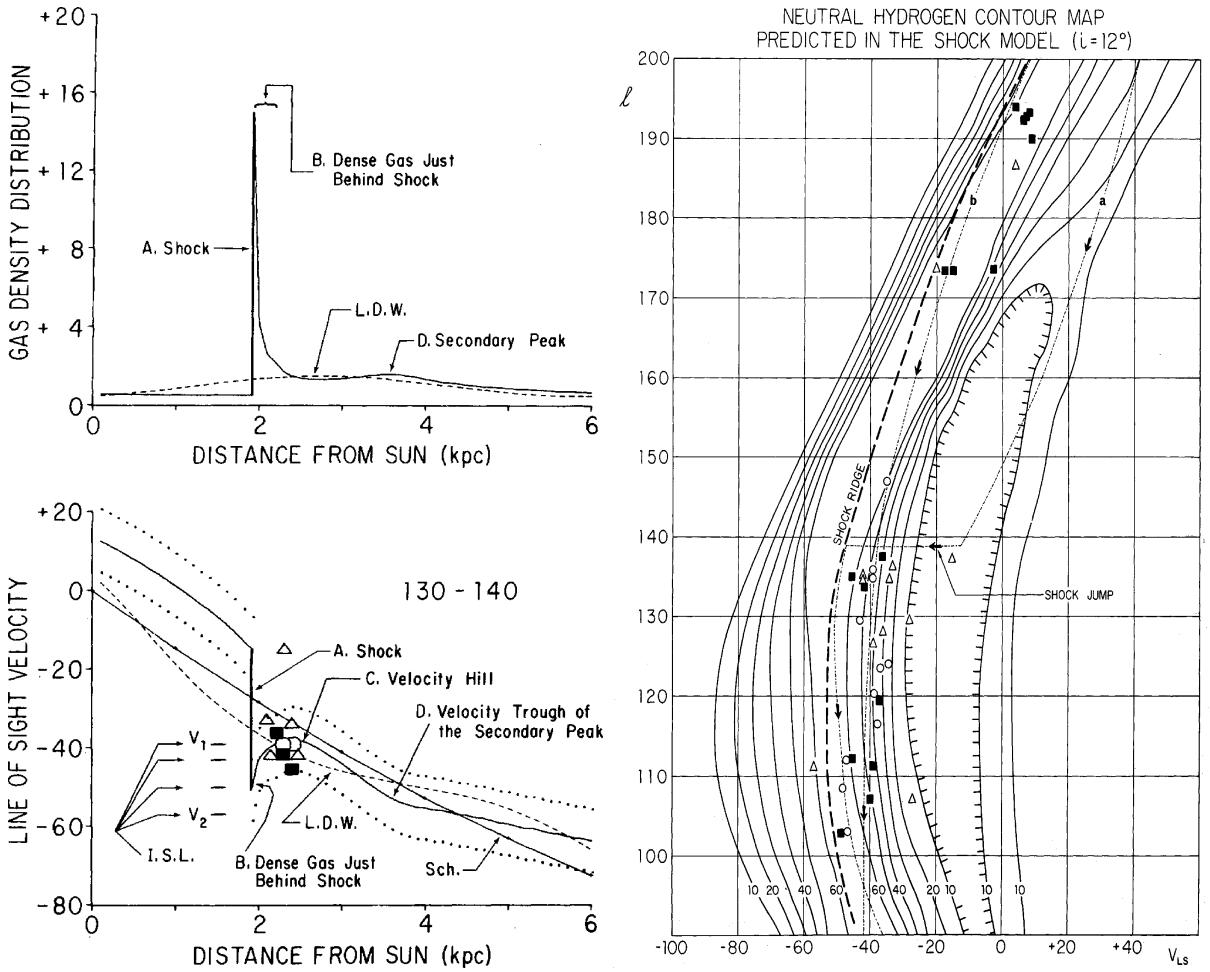

Fig. 9.— Plots from Roberts' (1972) Figures 3 and 6 that illustrate his two-arm spiral shock (TASS) model, reproduced here with permission. *Left:* Gas density and LSR velocity vs. distance for a 12° pitch angle and $130° \leq \ell \leq 140°$. The observer is at left; gas flows from left to right, overtaking the Perseus arm from behind. The smooth solid line is from an equilibrium Schmidt (1965) rotation model. The dashed line shows a linear density wave model, and the solid line with the discontinuity at $\sim$ 2 kpc is the TASS model, with a $\pm 8\,\mathrm{km\,s^{-1}}$ dispersion band marked with dotted lines. The symbols mark various spiral arm tracers. *Right:* (ℓ, v) plot of predicted gas emission brightness temperature for the same TASS model. The dashed line marks the "shock ridge" (region B in the lower-left panel), where dense gas occurs just behind the shock. For full details, see Roberts (1972).

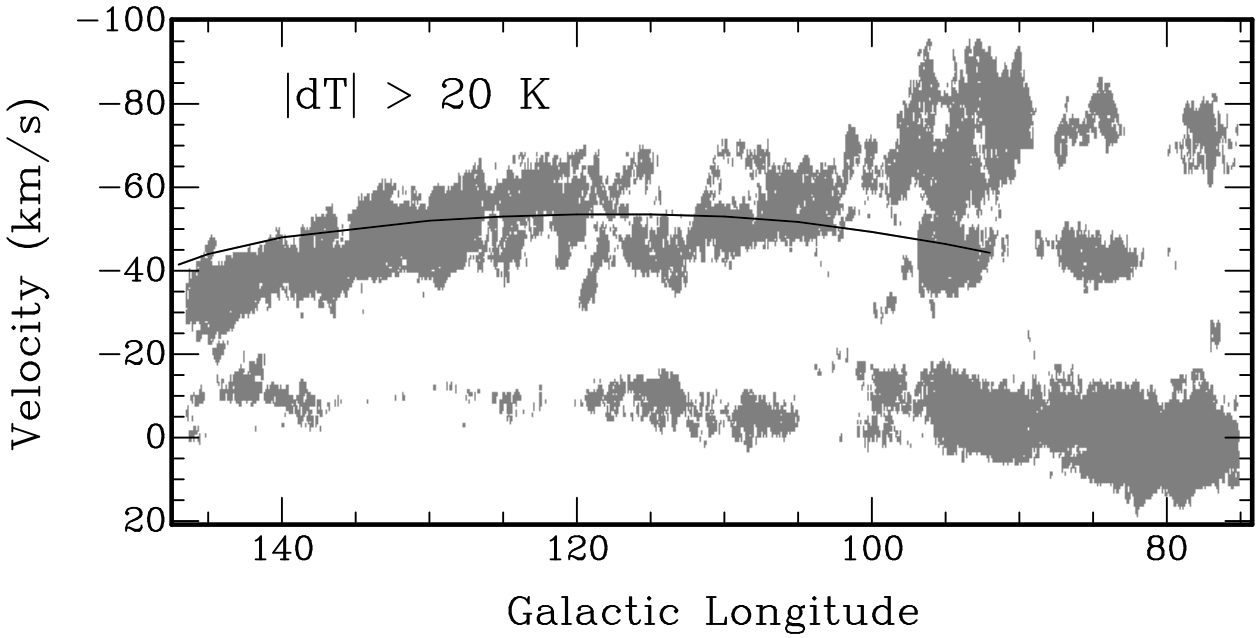

Fig. 10.— (ℓ, v) distributions of CGPS HISA projected over all b for a minimum voxel amplitude of $|\Delta T|_{min} = 20$ K. The Perseus arm spiral shock ridge of Roberts (1972) is marked over all longitudes that overlap with the CGPS (see Fig. 9).